Journal of Applied Geophysics 247 (2026) 106130

Contents lists available at ScienceDirect

Journal of Applied Geophysics

journal homepage: www.elsevier.com/locate/jappgeo

Impact of non-1D Earth on FDEM measurements and the performance of PWI and LCI Inversions

Maria Carrizo Mascarell [a,*], Dieter Werthmüller [a,b], Evert Slob [a]

[a] Delft University of Technology, Section of Applied Geophysics and Petrophysics, Faculty of Civil Engineering and Geosciences, Stevinweg 1, Delft, 2628CN, The Netherlands

[b] Federal Institute of Technology Zurich, Geothermal Energy and Geofluids, Department of Earth and Planetary Sciences, Sonneggstrasse 5, Zurich, 8092, Switzerland

ARTICLE INFO

Keywords:
Electromagnetic induction
FDEM
Laterally constrained inversion

ABSTRACT

Subsurface electrical conductivity models from frequency-domain electromagnetic (FDEM) induction measurements are often derived using computationally efficient one-dimensional piecewise inversion (PWI) approaches. However, PWI does not account for lateral conductivity variations or the measurement overlap between adjacent soundings, which can limit model estimation accuracy. Laterally constrained inversion (LCI) introduces smoothness constraints to reduce lateral variability between neighbouring models, potentially improving continuity. In this study, both PWI and LCI use a 1D forward function, assuming a horizontally layered earth, and a horizontally laying rigid boom instrument, to perform the estimations This study presents a detailed analysis of how various 2.5D and 3D conductivity distributions, including topographic variations and instrument pitch angle, affect FDEM measurements. We examine how these measurement distortions propagate into PWI and LCI inversion results. Under ideal conditions, such as flat terrain, no instrument tilt, and simple two-layer models, both methods recover accurate conductivity structures, with LCI offering little advantage in accuracy. When topography is introduced, however, distortions occur even at slopes as small as 2°, and both methods show degraded performance, particularly in 3D scenarios. In the field example, LCI produces smoother and more stable results than PWI in the presence of noise, but its assumption of lateral smoothness can be restrictive in geologically complex settings. Our findings show that both inversion strategies are sensitive to topographic and 3D effects, and that error propagation significantly influences inversion reliability. These results highlight the need for improved methodologies capable of handling realistic acquisition conditions and measurement uncertainties in FDEM surveys.

1. Introduction

Ground-based frequency domain electromagnetic (FDEM) induction soundings with loop-loop configurations are commonly used for mapping electric conductivity inside the subsurface. Electrical conductivity models estimated with this geophysical measurement are used in various applications, such as geologic mapping, mining, water exploration, precision farming, and archeology. Single-frequency, multi-configuration sensors can simultaneously measure different volumes of subsurface investigation. The resulting measurements are commonly used to image the subsurface through data inversion.

It has been suggested with numerical examples that for a 2-layered horizontal subsurface, the inversion problem is unique for a specific instrument configuration (Carrizo Mascarell et al., 2024b). This allows for the estimation of electrical conductivity models from loop-loop configuration FDEM measurements using a 1D piecewise layered medium approach, as they are computationally easy to solve (Heagy et al., 2017; Kiyan et al., 2022; McLachlan et al., 2021). However, FDEM measurements are influenced by a volume of the subsurface that contains lateral and vertical variations in three dimensions. This might present a limitation for an accurate representation of the true distribution of the electrical conductivity of the subsurface. Moreover, the piecewise 1D approach presents a lack of continuity between adjacent soundings when, in reality, there is an overlap of the subsurface volumes that are influencing the measurements.

A way to tackle the lack of continuity between 1D estimations is to introduce prior information through smoothness constraints, to limit the variability between the parameter values characterizing the adjacent 1D models (Constable et al., 1987). This inversion method is called Laterally Constrained Inversion (LCI), see, e.g., Auken and Christiansen

* Corresponding author.
E-mail addresses: maria.carrizo.mascarell@gmail.com (M.C. Mascarell), dieter.werthmuller@eaps.ethz.ch (D. Werthmüller), e.c.slob@tudelft.nl (E. Slob).

https://doi.org/10.1016/j.jappgeo.2026.106130
Received 24 March 2025; Received in revised form 8 December 2025; Accepted 21 January 2026
Available online 29 January 2026

(2004). Some examples of FDEM data are shown in Monteiro Santos (2004), Christiansen et al. (2016) and Klose et al. (2022).

Previous studies have mentioned the limitations of the PWI and LCI methods in reproducing 2D and 3D structures, since they rely on 1D forward modelling (Ley-Cooper et al., 2010; Silic et al., 2015). Several corrective approaches have been proposed to address these issues (Bai et al., 2021; Deleersnyder et al., 2022). Moreover, full 3D inversion of electromagnetic measurements has also been subject to research in the past decade (Alumbaugh and Newman, 2000; Oldenburg et al., 2020; Zhang et al., 2021). However, it requires a significant amount of computational resources that can be prohibitive.

In this study, we investigate how different forms of three-dimensional variability in subsurface electrical conductivity affect FDEM measurements. Our goal is to determine to what extent the 1D forward model is sufficient to reproduce measurements in 2.5D/3D earth models. To this end, we demonstrate how the differences in the measurements impact the accuracy of PWI and LCI inversion results in noise-free conditions, where 1D forward modelling assumptions are considered. To better approximate field conditions, we simulate dipping interfaces, instrument pitch angle, and realistic topography, where the instrument follows the slope of the air-subsurface interface. We then evaluate how these effects influence model estimations in a series of numerical examples, culminating in a discussion of the results and their implications for field surveys.

2. Theory

The FDEM instrument holds two components: a transmitter coil T_x and a receiver coil R_x. The system uses an alternating current flowing in the transmitter coil as a source to create an alternating primary magnetic field $\mathbf{H}^{\mathrm{p}}$, where the magnetic dipole is perpendicular to the transmitter coil plane T_x. This time-varying flux produces an electromotive force inducing eddy currents in the conductive materials of the subsurface as described by Faraday's law:

$$\nabla \times \mathbf{E} = -\mu \frac{\partial \mathbf{H}}{\partial t}, \tag{1}$$

where $\mathbf{E}$ is the vector electrical field strength, $\mathbf{H}$ is the vector magnetic field strength, μ is the magnetic permeability and t is time. The eddy currents in the subsurface generate an alternating secondary magnetic field $\mathbf{H}^{\mathrm{s}}$. The total magnetic field strength is the sum of the primary and secondary magnetic fields ($\mathbf{H} = \mathbf{H}^{\mathrm{p}} + \mathbf{H}^{\mathrm{s}}$). The time-varying fluxes of the magnetic fields $\mathbf{H}^{\mathrm{p}}$ and $\mathbf{H}^{\mathrm{s}}$ pass through the receiver coil, inducing a voltage that the instrument can measure. Since the primary field $\mathbf{H}^{\mathrm{p}}$ is known, FDEM instruments can provide the mutual impedance ratio between $\mathbf{H}^{\mathrm{s}}$ and $\mathbf{H}^{\mathrm{p}}$, which contains information about the subsurface conductivity.

FDEM multi-configuration instruments provide apparent conductivity σ_a measurements that are transformed into *quadrature* ($\mathbf{Q}$) values (McNeill, 1980), and *in-phase* ($\mathbf{IP}$) measurements. In this study, we use an FDEM instrument configuration, as shown in Fig. 1, where *quadrature* and *in-phase* measurements are obtained for each coil-coil configuration.

For a horizontally layered earth with two layers, the model parameters are defined as

$$\mathbf{m}_{true} = [\sigma_1, \sigma_2, h_1], \tag{2}$$

where σ_1, σ_2 are the electrical conductivities of the two layers, and h_1 is the thickness of the first layer. The corresponding data vector is

$$\mathbf{d}_{obs} = [\mathbf{Q}^{\mathrm{H}}, \mathbf{Q}^{\mathrm{P}}, \mathbf{Q}^{\mathrm{V}}, \mathbf{IP}^{\mathrm{H}}, \mathbf{IP}^{\mathrm{P}}, \mathbf{IP}^{\mathrm{V}}], \tag{3}$$

where the superscripts H, V and P indicate the coil-coil orientation.

3. Methodology

In this section, we describe the methodologies used to invert electrical conductivity models using FDEM measurements. We compare the results of two inversion methodologies: Piecewise 1D Inversion (PWI) and Laterally Constrained Inversion (LCI). Both inversion methods use 1D horizontally layered forward modelling described in the following section.

3.1. Forward modelling

For the 1D forward modelling, used in the PWI and LCI methods, we assume a horizontally layered medium and use the wavenumber-frequency formulation given by Wait (1982). We use a digital linear filter provided by Werthmüller (2017) for the Hankel transform to the space-frequency domain. Further details of the 1D forward modelling can be found in Carrizo Mascarell et al. (2024b). We make two key assumptions: (1) The medium is horizontally layered. (2) The instrument coils are positioned at the same height (meaning pitch angle zero). These assumptions are presented as Case (a) in Fig. 3. Moreover, we used a 3D forward modelling scheme to simulate the data for the numerical examples in which the 1D assumptions do not hold, in order to realistically assess the impact of violating these assumptions. The scheme was created with the open source package *emg3d* presented in Werthmüller et al. (2019).

3.2. Piecewise 1D Inversion (PWI)

In the PWI method, we estimate each sounding location separately (see Fig. 2). FDEM measurements are inverted using the Gauss–Newton optimization presented by Günther et al. (2006) and implemented in the *pyGIMLi* package (Rücker et al., 2017) as described in Carrizo Mascarell et al. (2024b). This inversion uses internally the 1D forward modelling mentioned in Section 3.1.

The gradient-based optimization scheme uses the Gauss–Newton method to solve nonlinear least squares problems (Nocedal and Wright, 1999, p. 259–262) to minimize the following objective function.

$$\Phi_{\mathbf{m}} = \|\mathbf{C}_d(\mathcal{F}(\mathbf{m}) - \mathbf{d})\|_2^2 + \alpha\|\mathbf{C}_m(\mathbf{m} - \mathbf{m}_0)\|_2^2, \tag{4}$$

where $\mathcal{F}(\mathbf{m})$ is the forward operator, $\mathbf{C}_d$ and $\mathbf{C}_m$ are the data weighting and model constraint weighting matrices, $\mathbf{m}_0$ is the initial model, and α is a regularization term. The Gauss–Newton scheme to minimize this equation updates the model $\Delta\mathbf{m}_k$ in the kth iteration using

$$(\mathbf{J}^T\mathbf{C}_d^T\mathbf{C}_d\mathbf{J} + \alpha\mathbf{C}_m^T\mathbf{C}_m)\Delta\mathbf{m}^k = \mathbf{J}^T\mathbf{C}_d^T\mathbf{C}_d(\Delta\mathbf{d}^k) - \alpha\mathbf{C}_m^T\mathbf{C}_m(\mathbf{m}^k - \mathbf{m}^0), \tag{5}$$

where $\mathbf{J} = \frac{\partial\mathcal{F}(\mathbf{m})}{\partial\mathbf{m}}$, $\Delta\mathbf{d}^k = \mathbf{d} - \mathcal{F}(\mathbf{m}^k)$. The model vector $\mathbf{m}$ is updated iteratively following

$$\mathbf{m}^{k+1} = \mathbf{m}^k + \tau^k\Delta\mathbf{m}^k, \tag{6}$$

using a linear search parameter, τ, the superscript k indicates the iteration number. The linear search parameter τ is obtained by linear interpolation between the old and new model responses.

3.3. Laterally constrained inversion (LCI)

We carry out the LCI using the method introduced by Auken et al. (2005) and presented for FDEM measurements on a 2-layered earth in Carrizo Mascarell et al. (2024a). The LCI produces a simultaneous inversion of adjacent sounding locations to obtain quasi-layered subsurface models (see Fig. 2). The basic assumption of the LCI concept is that the lateral constraints are considered prior information on the spatial variability in the area. Lateral continuity is imposed, regularizing the inverse problem by constraining neighbouring model parameters. We implement the previously mentioned Gauss–Newton optimizer, also used for the LCI method by Thalhammer (2022). This inversion also uses the 1D forward model mentioned for PWI.

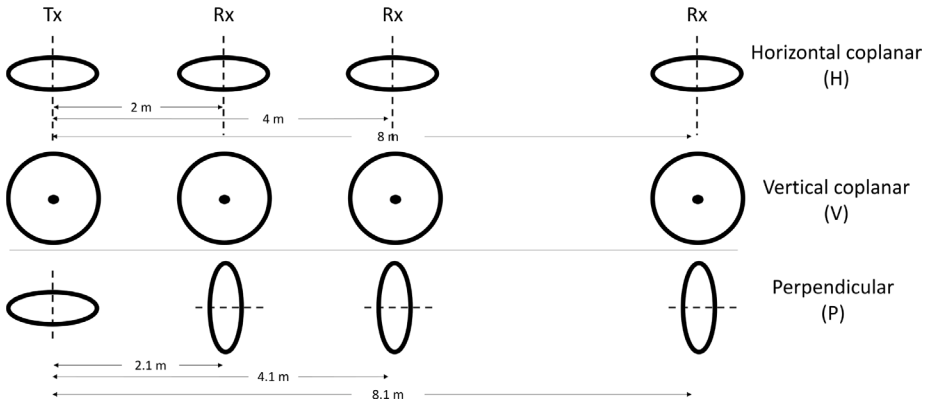

Fig. 1. FDEM instrument configuration used in this study.

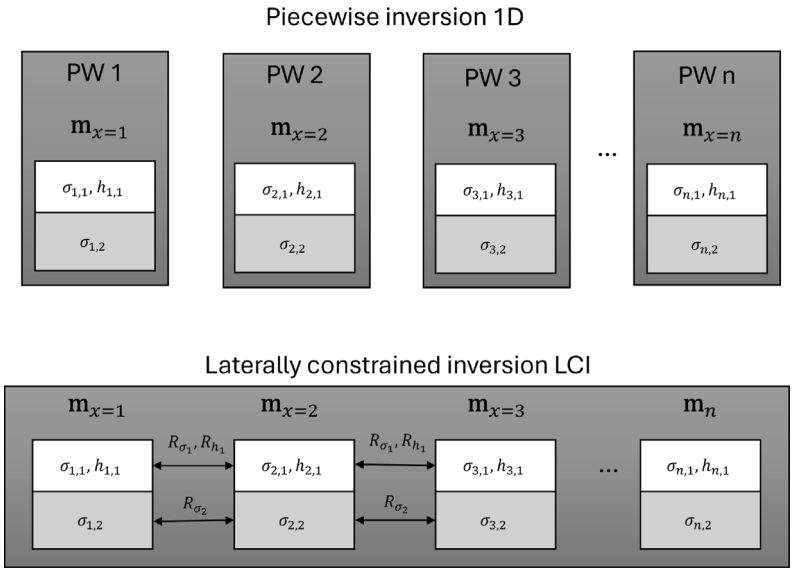

Fig. 2. Inversion methods: In the PWI method, each sounding position x is estimated separately. In the LCI method, all of the models are inverted simultaneously using spatial constraints between adjacent models **R**.
Source: Modified from Auken et al. (2005).

The objective function is expressed as

$$\Phi_{\boldsymbol{m}} = \|\boldsymbol{C}_{\mathrm{d}}(\mathcal{F}(\mathbf{m}) - \mathbf{d})\|_2^2 + \alpha\|\mathbf{R}\mathbf{C}_{\mathrm{m}}(\mathbf{m} - \mathbf{m}_0)\|_2^2. \tag{7}$$

The roughening matrix **R** applies the lateral constraints as

$$\mathbf{R}\delta\mathbf{m} = \delta\mathbf{r} + \mathbf{e}_{\mathrm{r}}, \tag{8}$$

where $\mathbf{e}_{\mathrm{r}}$ represents the error on the constraints, $\delta\mathbf{r}$ the identity between parameters linked by constraints, and $\delta\mathbf{m} = \mathbf{m} - \mathbf{m}_0$. The roughening matrix **R** is sparse, containing only diagonals of 1 and −1 for the constrained model parameters (as in Eq. (9)). Each matrix row enforces a constraint between two model parameters,

$$\mathbf{R} = \begin{bmatrix} 1 & 0 & \dots & 0 & -1 & 0 & \dots & 0 & 0 & 0 \\ 0 & 1 & 0 & \dots & 0 & -1 & 0 & \dots & 0 & 0 \\ \vdots & & & & & \vdots & & & & \vdots \\ 0 & 0 & 0 & \dots & 0 & 1 & 0 & \dots & 0 & -1 \end{bmatrix}. \tag{9}$$

The objective function in Eq. (7) is minimized also using *pyGIMLi* in a Gauss–Newton scheme (Günther et al., 2006). The model update is calculated by

$$\Delta\mathbf{m}^k = (\Re[\mathbf{J}^\dagger\mathbf{C}_d\mathbf{J}] + \mathbf{R}\mathbf{C}_m)^{-1}(\Re[\mathbf{J}^T\mathbf{C}_d\delta\mathbf{d}^*] + \alpha\mathbf{R}\mathbf{C}_m\delta\mathbf{m}), \tag{10}$$

where † indicates the complex conjugate transpose and the symbol * indicates complex conjugation. It is clear if we compare Eqs. (4) and (7) that the PWI method is equivalent to the LCI method in the case where no constraints are imposed by a roughening matrix **R**.

4. Error analysis on measurements due to 3D effects

In this section, we present several cases where the assumptions of the 1D forward model mentioned in Section 3.1 are violated: the subsurface is not horizontally layered, or the instrument is not positioned at the same height. These cases are shown in Fig. 3.

Case (a): Horizontal earth model

In this case the earth model is horizontally layered and the instrument lays parallel to the ground. The instrument coils are all at the same height.

Case (b): Air-subsurface interface with respect to the instrument is not zero

This case (see Fig. 3) illustrates when one of the two 1D forward function assumptions is violated. Either the instrument coils are at equal height and the air-subsurface interface is not horizontal. Or the air-subsurface interface is horizontal, but the instrument is at non-zero pitch angle. These cases are equivalent geometrically, representing an angle of the instrument with the air-subsurface interface. We show in Fig. 4 the measurements corresponding to the instrument configuration

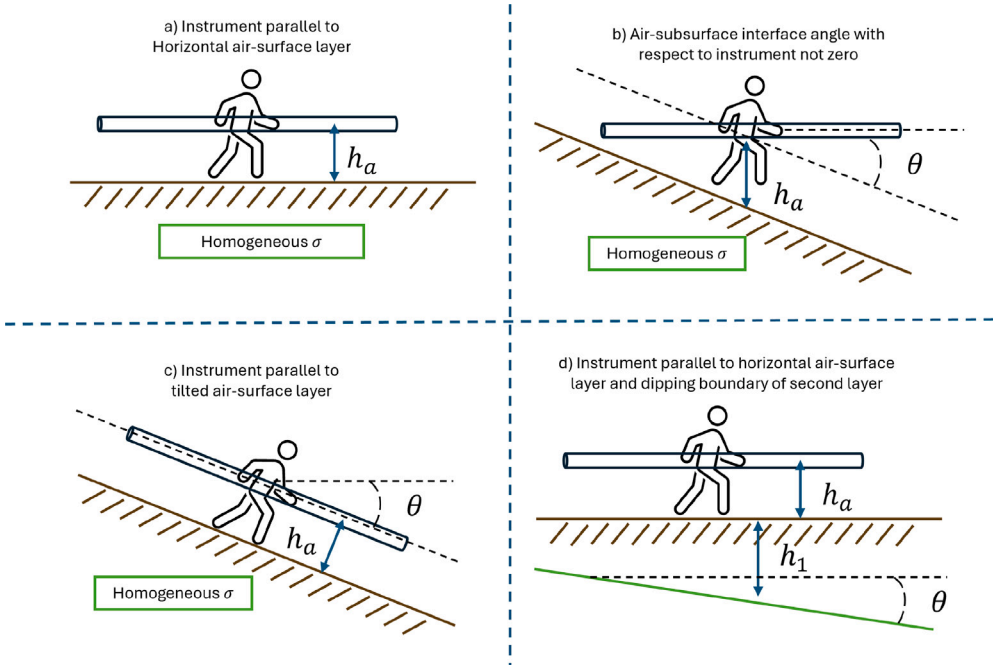

Fig. 3. Illustration of four possible configurations of instrument geometry with respect to subsurface geometry. Case (a): Horizontally layered earth, instrument coils at the same height. Case (b): Air-subsurface interface with respect to the rigid-boom axis is not zero. Case (c): Dipping air-subsurface interface, instrument parallel. Case (d): Dipping second interface, rigid boom axis horizontal.

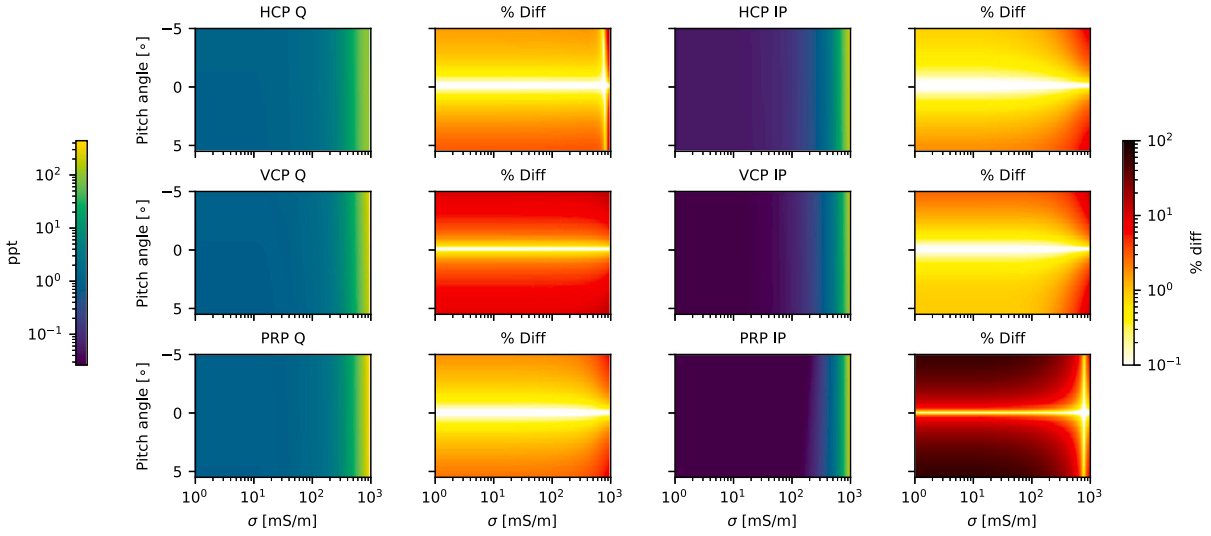

Fig. 4. Case (b): Effect on the measurements due to pitch angle for offset 8 m. The first and third columns show the measurements and the second and fourth columns show the respective differences with a 0° pitch.

at 8 m offset, for a wide range of homogeneous half-spaces with increasing degrees of angle between instrument and air-subsurface interface. In the figure it is clear that the measurements are distorted with increasing pitch angle. The *quadrature* values of VCP and *in-phase* values of the PRP geometry are the most affected and differ largely with increasing pitch angle in all offsets and electrical conductivities of the halfspace. These results suggest that, if the rigid boom is positioned horizontally, the dip of the air-surface interface creates distortions of more than 5% in the measurements with only 2° dip. This effect worsens with increasing offset. It is possible that these measurement distortions will negatively impact the estimation of electrical conductivity models. The results for the remaining offsets are presented in the Supplementary Material (Carrizo Mascarell et al., 2025).

Case (c): Dipping air-subsurface interface

In case (c) we show the influence on the FDEM measurements of breakdown of both 1D forward function assumptions: the air-subsurface interface is not horizontal, and the instrument lies parallel to this interface, thus, the instrument coils are not at equal height. In Fig. 5 the measurement deformations due to the violation of both assumptions are plotted for a range of different electrical conductivity halfspaces at 8 m offset. It is clear that for increasing dip angle the measurement is increasingly distorted. The VCP *quadrature* and the VCP and PRP *in-phase* components show the largest deviations with only 2–3° of dip, in similar manner to case (b). The results for the remaining offsets are presented in the Supplementary Material (Carrizo Mascarell et al., 2025).

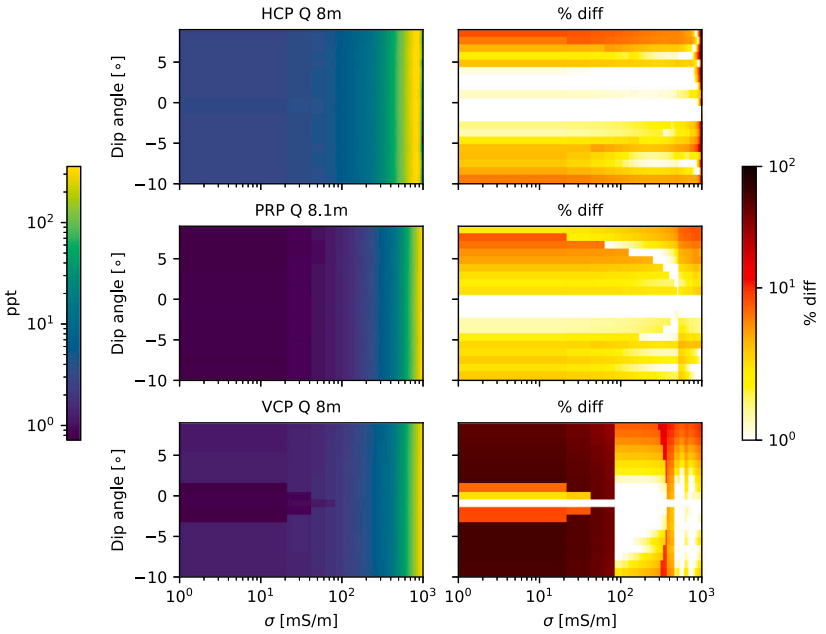

(a) *Quadrature* values.

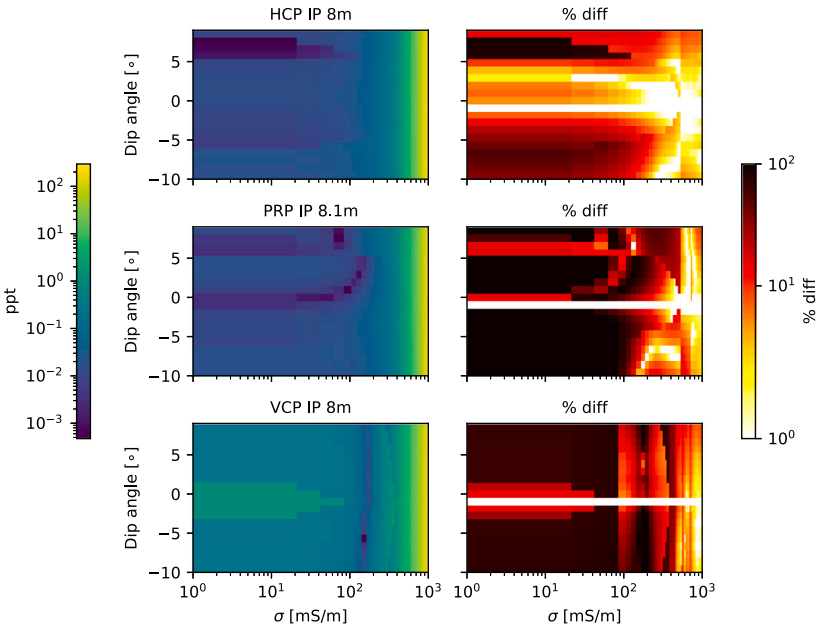

(b) *In-Phase* values.

Fig. 5. Case (c): Effect of dipping topography for the coils at 8 m offset. The left column shows the measurements. The right columns presents the measurement difference percentage.

Case (d): Dip of the second interface

In case (d) the subsurface geometry causes the breakdown of the first 1D assumption for a 2-layered model, since the interface between the first layer and the second layer is not horizontal. We show the results for eight 2-layered models presented in Table 1 with different electrical conductivity contrasts. The upper conductive cases results are presented in Fig. 6 and the upper resistive cases are shown in Fig. 7. Overall, for the upper conductive and upper resistive cases the measurement distortions are similar for different electrical conductivity contrasts. For all the upper conductive cases, the VCP *in-phase* measurements are the most affected. However, for the upper resistive cases, the PRP *in-phase* measurements are highly distorted (more than 20% of difference) with only 2–3° of dip in the second interface.

5. Robustness of the inversion methods

In the previous section, we showed how the FDEM measurements are quite rapidly distorted with the breakdown of the 1D forward function assumptions in the presence of variations of not-horizontally layered geometry (even with only 2–3° of difference), or due to the instrument pitch. In this section, we will test how these distortions affect the PWI and LCI results, in noise-free conditions. We present examples for two-layered earth models, for a horizontally layered earth and modelled with the instrument configuration presented in 1, with all coils at the same height. It is important to mention that using a 2-layered model parameterization substantially constrains the solution

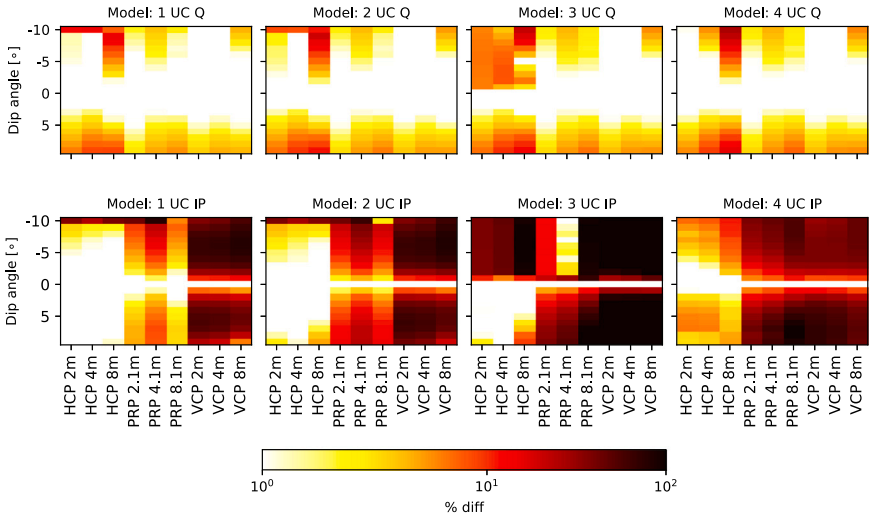

Fig. 6. Case (d): Measurement distortion for a dipping second interface for upper conductive 2-layered models. Top row: *Quadrature* measurements. Bottom row: *In-Phase* measurements.

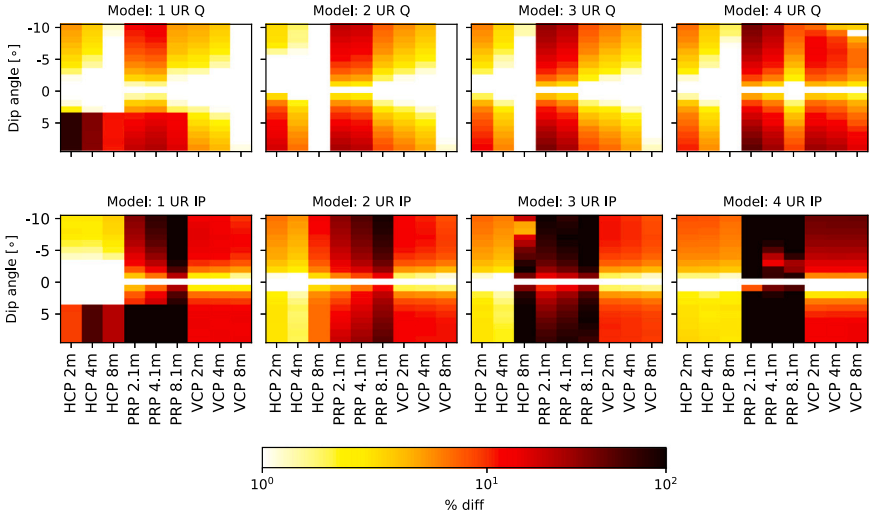

Fig. 7. Case (d): Measurement distortion for a dipping second interface for upper resistive 2-layered models. Top row: *Quadrature* measurements. Bottom row: *In-Phase* measurements.

space, and thus limits the capability of the inversion method to explain the data. We also show a single case with added noise to the measurements to illustrate their impact in the inversion methods.

First, we apply the method for numerical 2.5D models (3D models where the third dimension projects the 2D model) and 3D models. Afterwards, we test the methods in a field case. Example 0 is a base case where the measurements are calculated using 1D forward modelling. In the following numerical examples, the measurements were simulated using 3D forward modelling. Examples 1 to 3 are 2.5D models (where the third dimension is a projection of a 2D cross-section). Examples 4 and 5 are 3D models, with variations in the electrical conductivity distributions in 3 dimensions.

Example 0. 1D forward modelled measurements

In this case, we show the results of the PWI and LCI methods for Model 4 in Table 1 for the upper conductive contrast. This case is shown as a base result to demonstrate the capabilities of the inversion methods when the measurements 1D assumptions are not broken. The estimation results are presented in Fig. 8. The data fit is presented in Fig. 9. It is clear that the fit of the models is very accurate. The measurements are reproduced with less than 1% error. The measurements are shown in ppt notation, representing parts per thousand.

Table 1
Electrical conductivity (EC) distribution in 2-layered earth numerical cases.

Model	Upper conductive layer		Upper resistive layer	
	Top EC [mS/m]	Bottom EC [mS/m]	Top EC [mS/m]	Bottom EC [mS/m]
1	200	20	20	200
2	400	20	20	400
3	800	20	20	800
4	1600	20	20	1600

Example 1. Fixed dip of the second interface

We applied both inversion methods to 2-layered models with different electrical conductivity contrasts presented in Table 1 and increasing dip. The inversion results for two cases are presented in Figs. 10 and 12 (the results for all examples in Table 1 are provided in the Supplementary Material Carrizo Mascarell et al., 2025). The poor estimation of the lower layer, in the upper conductive cases, can be explained by the low sensitivity of the measurement to the resistive part of the subsurface. However, we also see erratic estimations from PWI for Models 3 and 4 for a 10° dip. In Fig. 11, we can see that the response of the PWI estimation does not differ more than 20% error

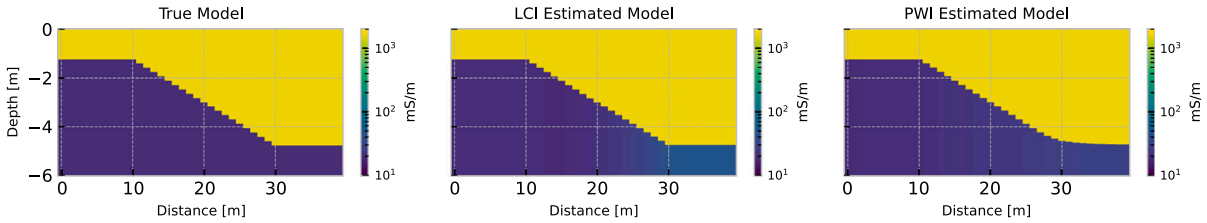

Fig. 8. Results of inversion methods for Model 4 using 1D forward modelled measurements.

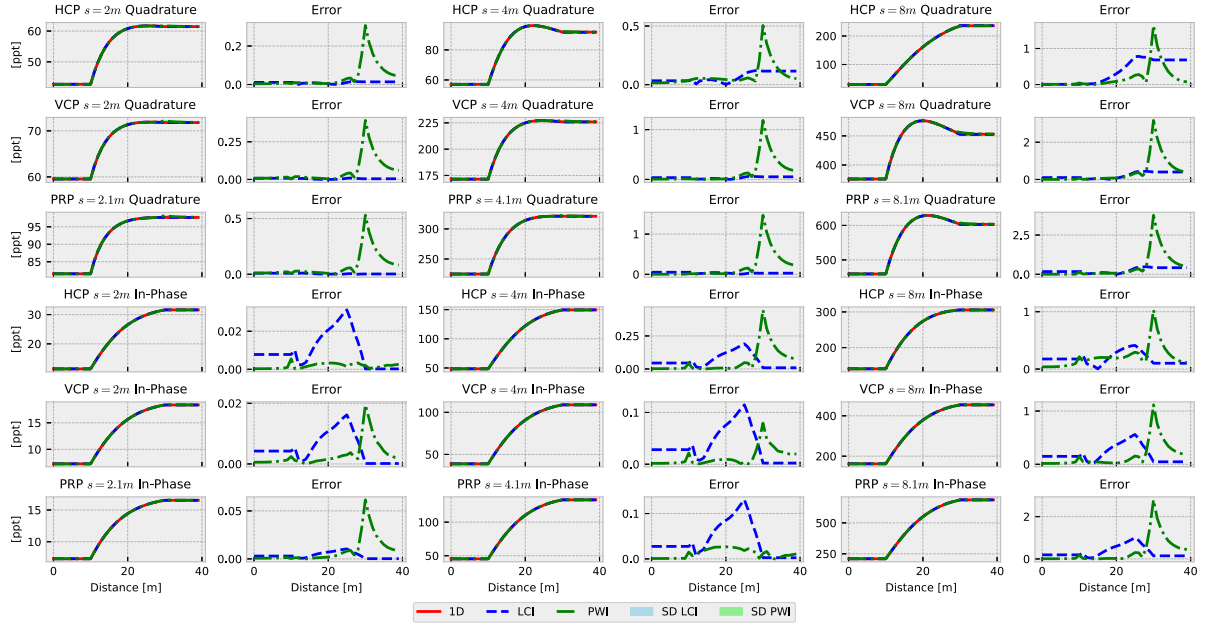

Fig. 9. Measurements corresponding to the results of Fig. 8. The first, third and fifth column show the data values. The second, fourth and sixth column show the error. The black line represents the measurements of the true model using the 1D forward function. The red line corresponds to the 3D forward function. The blue and green lines correspond to the 1D forward function response of the LCI and PWI estimated models, respectively.

with respect to the true measurements. However, we observe a much larger difference (larger than 100% in some positions) between the true measurements, simulated in 3D, with respect to their respective 1D forward modelled measurements, especially for the 8 m offset. With the PWI, the measurement distortions in this case negatively affect the possibilities of obtaining accurate estimations.

On the other hand, the results provided by both the PWI and LCI methods are similar in the upper resistive cases. In Fig. 13 the data fit for the upper resistive Model 4 for a 10° dip. In this case, we also observe that the 3D forward-modelled and 1D forward-modelled measurements differ significantly. This affects equally the LCI and PWI results, although not as strongly as in the upper conductive example.

A summary of the measurement errors for Model 1 in the upper resistive case is presented in Fig. 14. The figure shows that for increasing dip values, for every coil configuration, the 1D forward modelled measurements increase their mean error, as well as the standard deviation. This is also true for the responses calculated for the LCI and PWI estimates. In Fig. 15 we show the same analysis for Model 4, which has an increasing contrast between upper and lower layer conductivities. The mean error values are larger for these cases, since the conductivity also affects the estimations. Overall, for all cases the behaviour is similar, having increasing mean error values in the measurements with increasing dip angle for the interface between first and second layer.

With the intention of demonstrating the impact of noise in the result of the inversion methodologies, we estimate an example for Model 2 in the upper conductive case. In Figs. 16 and 17 the resulting models for increasing Gaussian random noise percentages in the measurements are shown. As expected, the estimates RMSE values increase with increasing noise in the measurements. It is clear that the LCI estimates show less spurious results, and the interface between first and second layer is better predicted.

In order to show the performance of the inversion methodologies in a complex 2-layered geological setting, where the subsurface is not nearly layered, we present an example in Fig. 18. Predictably, both inversion methodologies have inaccurate estimations. This is due to the fact that the measurements in these complex environments are not properly reproduced by the internal 1D forward modeller in the inversion schemes. Moreover, the LCI method holds constraints that assume a nearly layered geology, which is clearly not correct.

Example 2. Increasing dip of the second interface

In order to evaluate the effects of lateral variations in the LCI and PWI inversion methodologies, we introduced a numerical case, where the boundary between two electrical conductivity layers increasingly changes with distance, inspired on a similar analysis by Klose et al. (2022). The estimation results are shown in Fig. 19. We observe that the PWI estimated model shows a worsening of the estimation with increasing lateral variation of the boundary, especially in the peaks. However, it reproduces, on average, the position of the boundary. On the other hand, the LCI shows a smoothed result that does not reproduce the boundary position of the peaks. These results indicate that lateral variations will affect the PWI and LCI estimations when assuming a 1D horizontally layered earth in the inversion forward function, as in this case. The data fit between the true measurements and the estimation responses are presented in Fig. 20. We can see how the measurements are increasingly different to the true 3D measurements. However, the

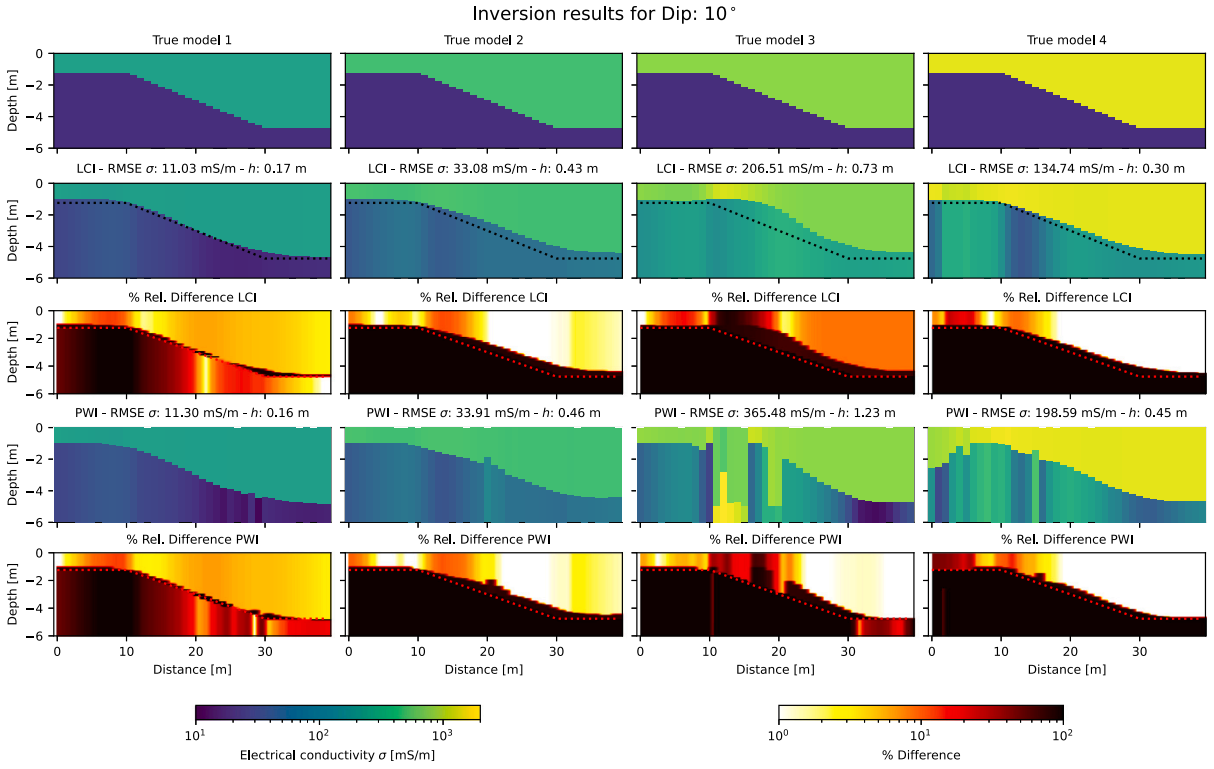

Fig. 10. Inversion results of 2-layered earth models with an upper conductive layer and a slope of 10° between positions X = 10 to X = 30. Upper row: True models. Second row: LCI estimated models. Fourth row: PWI estimated models. The third and fifth show the error percentage of the inversion results. In each model estimation, the RMSE of the model parameters is shown.

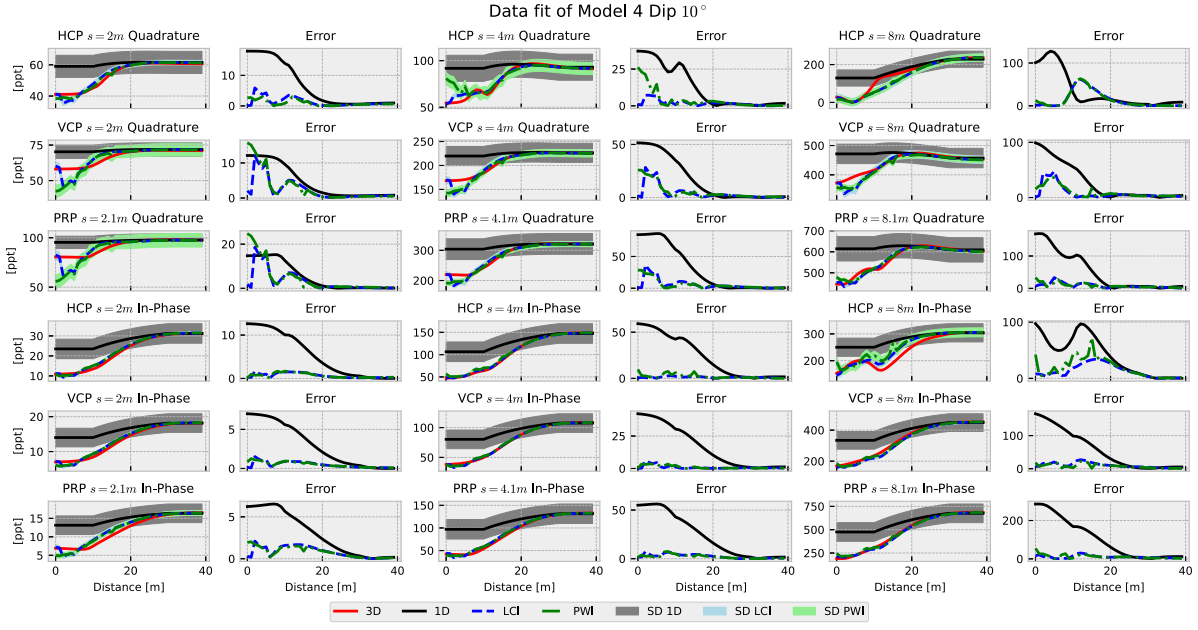

Fig. 11. Data fit results corresponding to Model 4 in Fig. 10. The first, third and fifth column show the data values. The second, fourth and sixth column show the error. The black line represents the measurements of the true model using the 1D forward function. The red line corresponds to the 3D forward function. The blue and green lines correspond to the 1D forward function response of the LCI and PWI estimated models, respectively. The blue and green shaded areas show the standard deviation of the LCI and PWI measurements errors, respectively.

difference between the 1D forward response of the model and the 3D measurements is even larger. Meaning the inversion methods try to fit the 3D data, jeopardizing the accuracy of the estimations. These numerical examples assumed an earth model without topography, with

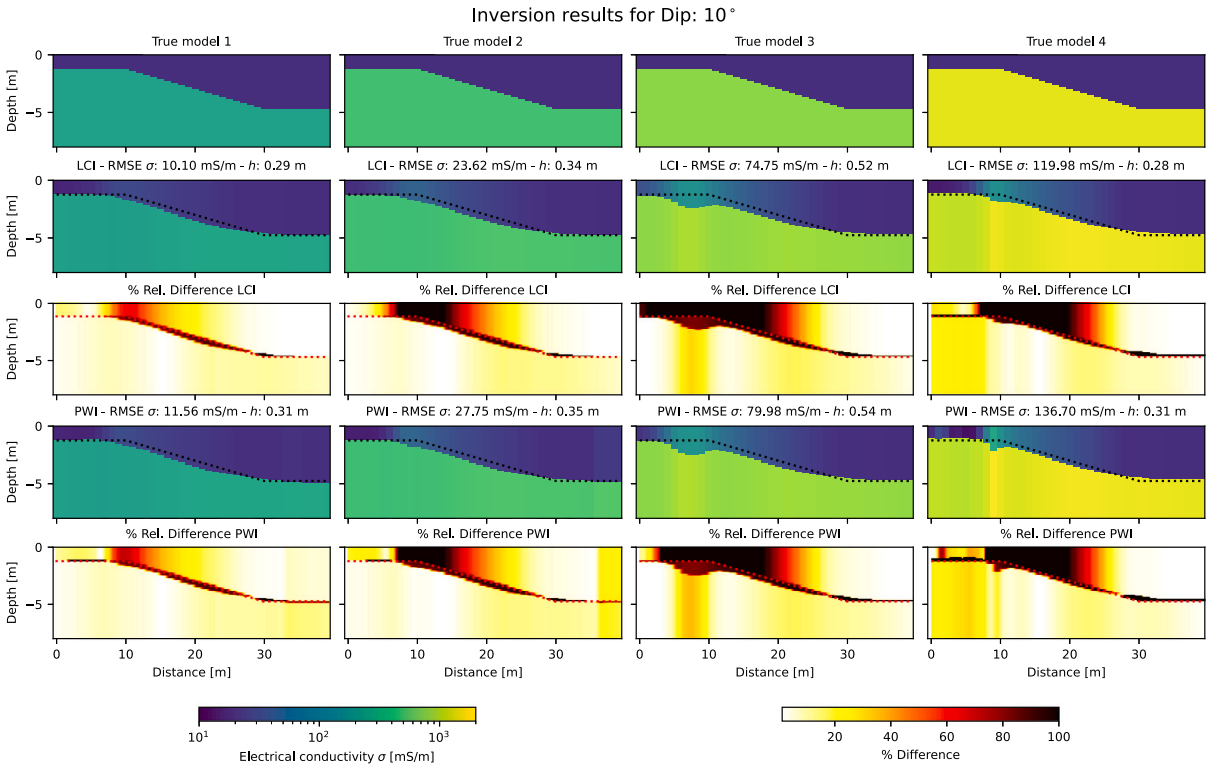

Fig. 12. Inversion results of 2-layered earth models with an upper resistive layer and a slope of 10° between positions X = 10 to X = 30.

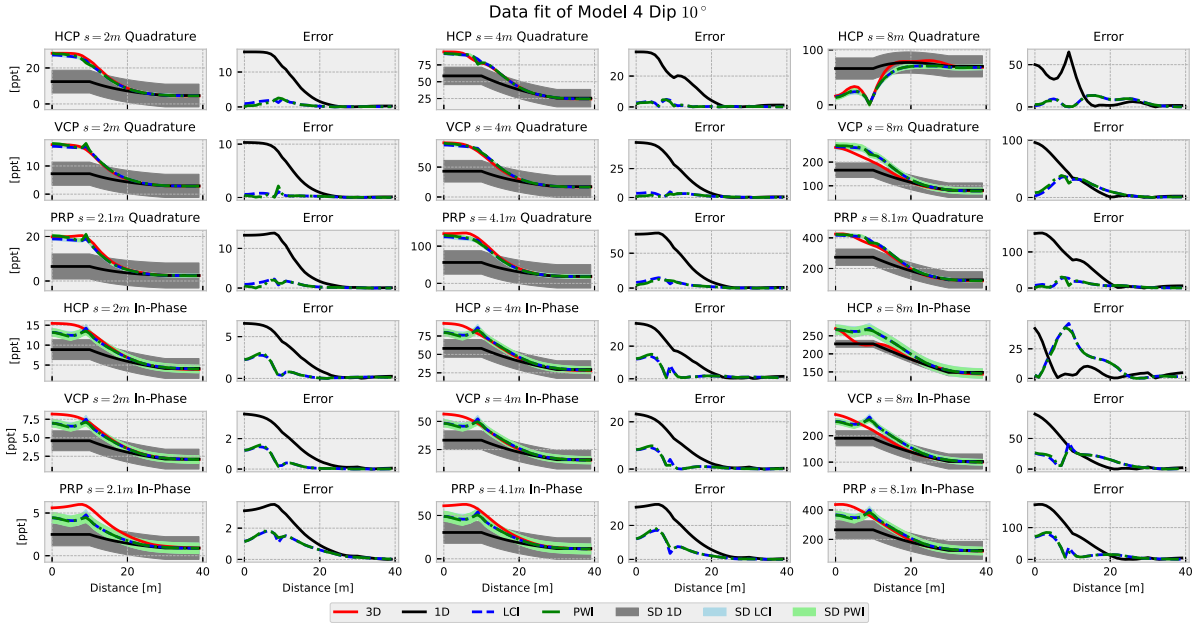

Fig. 13. Data fit results corresponding to Model 4 in Fig. 12.

an air-surface interface at $z = 0$, and the instrument lying parallel above the air-surface interface at a height $h_a = 0.3$ m.

Example 3. Increasing dip of the air-subsurface interface

To understand the effects of the dipping air-surface interface, we pose an instrument positioning case (Case (c) in Fig. 3) where we assume that the instrument is always parallel to the surface, with a height $h_a = 0.3$ m from the interface. The geometry of the instrument changes as we follow the topography while measuring, as in Fig. 21. We designed a numerical example shown in Fig. 23, in which the topography variations increase laterally. It is important to stress that the topography's maximum height is quite small (50 cm) and the figure aspect is exaggerated (~300:2), the maximum dips are 4°. The measurements are simulated using 3D forward modelling. In Fig. 22, we illustrate the positioning of the rigid boom in the simulated model.

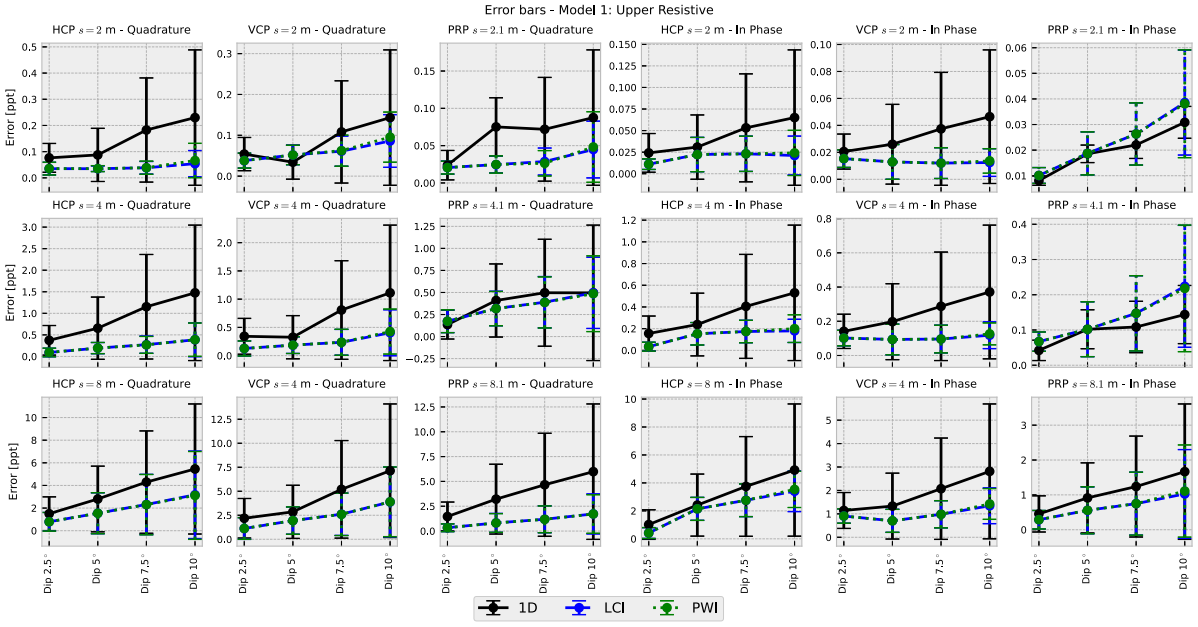

Fig. 14. Mean error values of the measurements for Model 1: Upper resistive case.

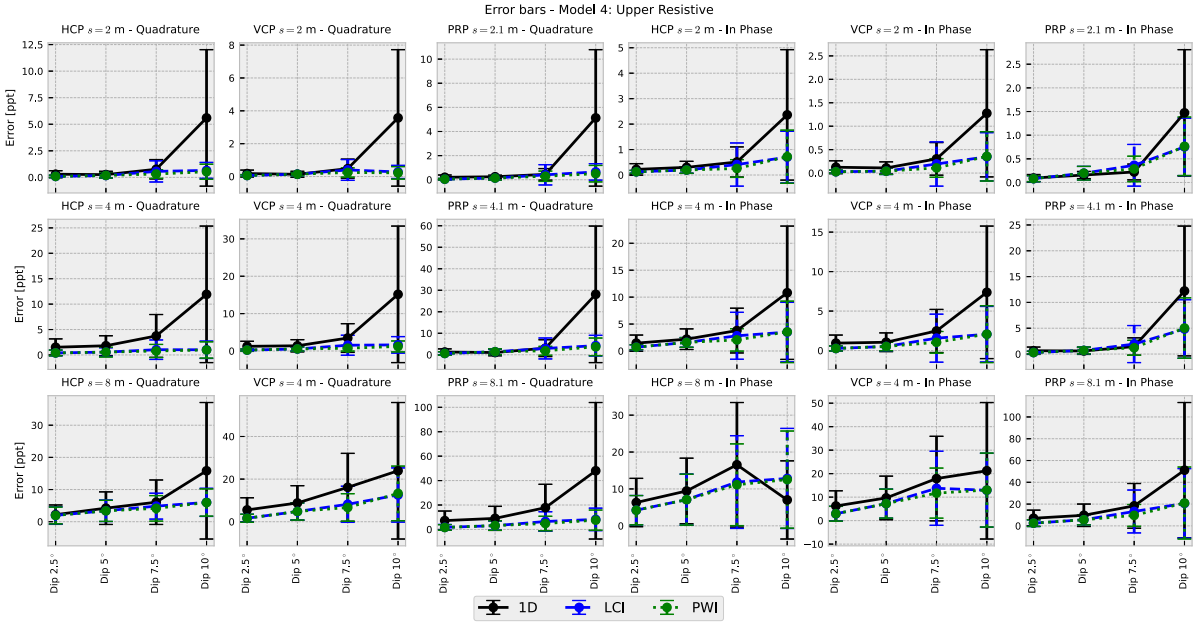

Fig. 15. Mean error values of the measurements for Model 1: Upper resistive case.

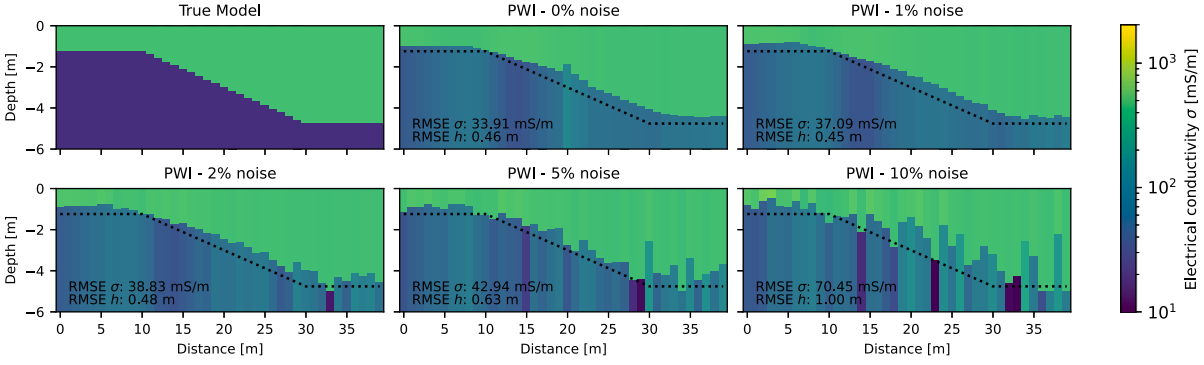

Fig. 16. Effects of noise in the measurements in the PWI inversion.

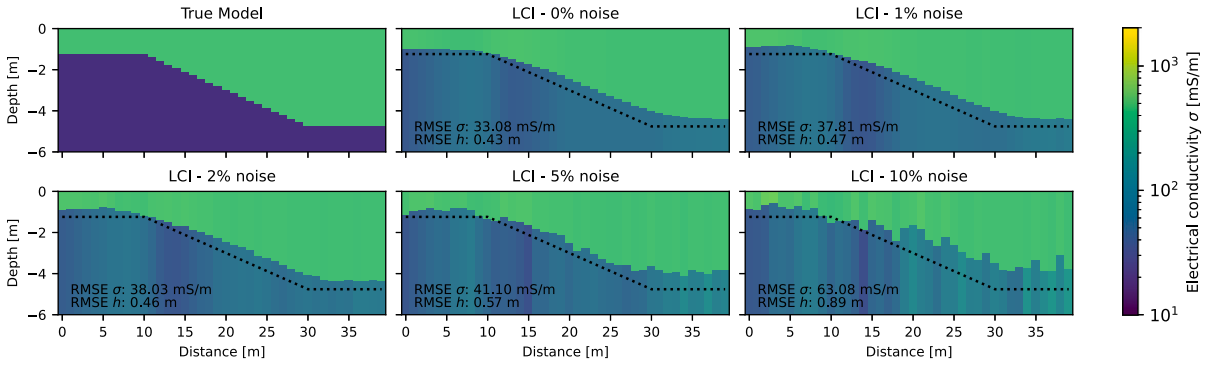

Fig. 17. Effects of noise in the measurements in the LCI inversion.

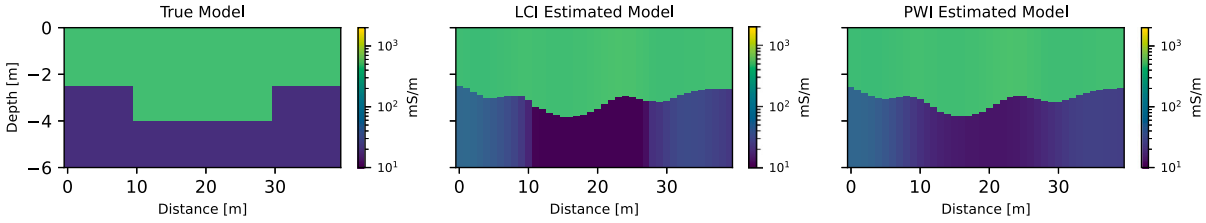

Fig. 18. Estimation results of the inversion methods for a complex geological distribution.

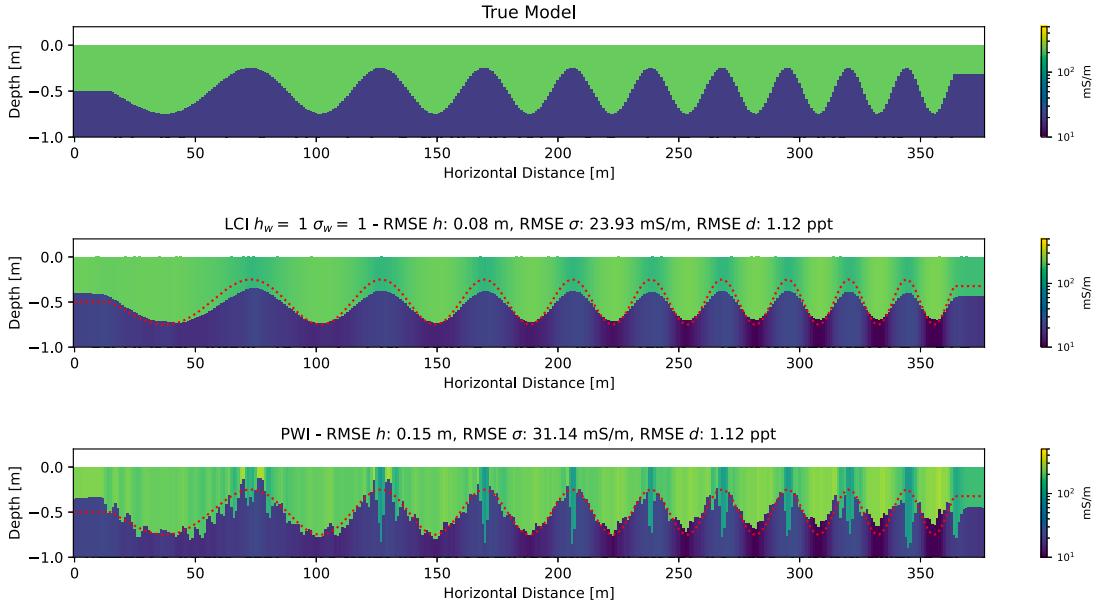

Fig. 19. Results of inversion methods for an increasing dip of the second interface. Top: True model. Middle: LCI estimated model. Bottom: PWI estimated model. The dotted red line indicates the true position of the interface. RMSE values of the estimated model parameters is presented.

The results from PWI and LCI methods shown in Fig. 23 present increasingly worse estimations with increasing topography dip. We infer that this is due to the increasing pitch angle in the instrument geometry, and that the air-surface interface is not parallel to the rigid boom, violating the assumptions of the 1D forward model. Therefore, the 1D forward function used in the inversion methods is not able to accurately represent the true model measurements. This is also shown by the inversion responses compared to the true measurements in Fig. 24. These results suggest that these gentle topography variations negatively impact the estimations when assuming an instrument parallel to the air-surface interface and a horizontally layered earth in the inversion methods.

Example 4. Channel feature

In this numerical example, we present a 3D model of a 2-layered earth with a channel feature. The measurements were simulated using the 3D forward modeller previously mentioned. The model contains the channel feature in the upper layer along with channel bars at each side and river plains, with an electrical conductivity of 50 mS/m, 30 mS/m and 10 mS/m, respectively. The bottom layer electrical conductivity is 100 mS/m. In Fig. 25, a map representation of the model parameters $(\sigma_1, \sigma_2, h_1)$ of the channel is presented, as well as the results of the LCI and PWI estimations. The maps show that PWI and LCI estimations are very similar in all parameters. The results of the estimations in cross-section Y = 10 m is presented in Fig. 26. The resulting estimations show alike results for LCI and PWI inversion methodologies for the

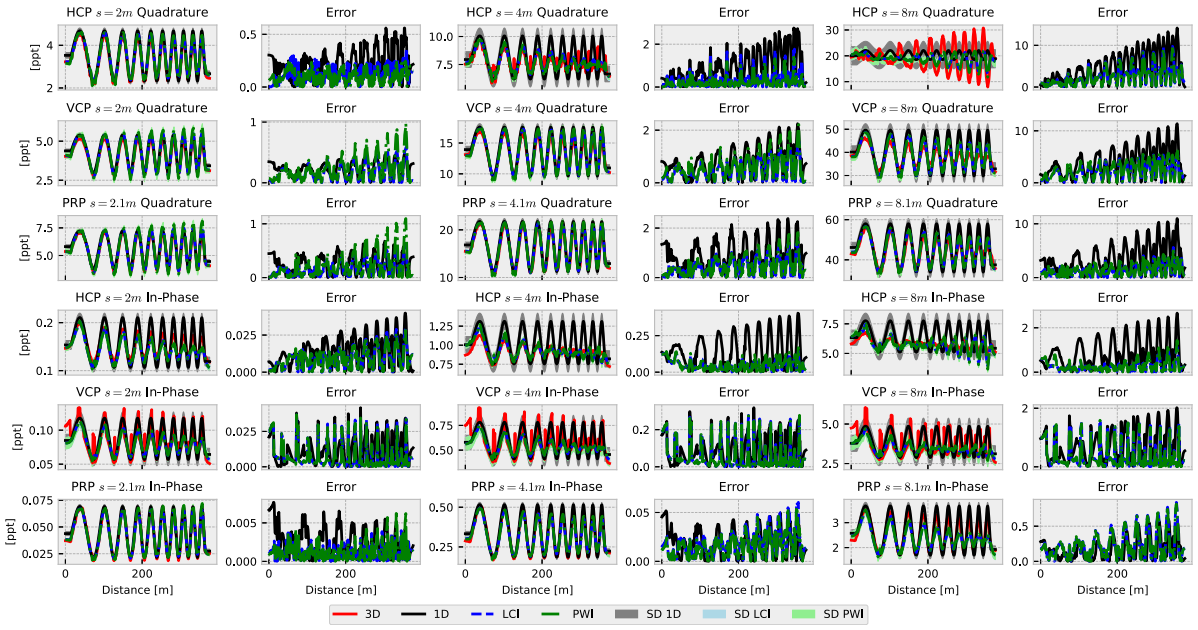

Fig. 20. Measurements corresponding to the model in Fig. 19 for all coil configurations and measurement components. The difference percentage with 3D measurements is shown below each measurement.

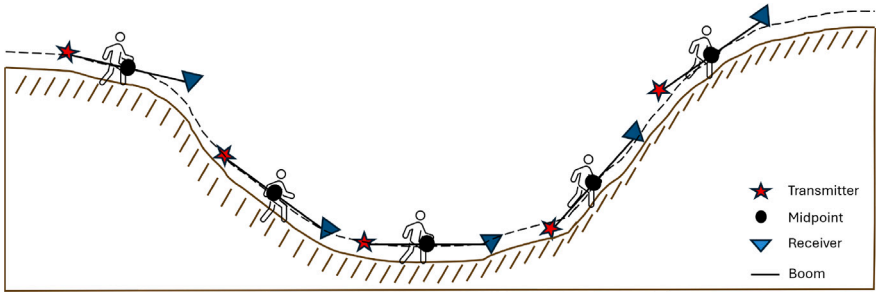

Fig. 21. Scheme of data acquisition with topography. The midpoint is positioned 0.3 m above the air-subsurface interface. The instrument pitch follows the dip of the slope.

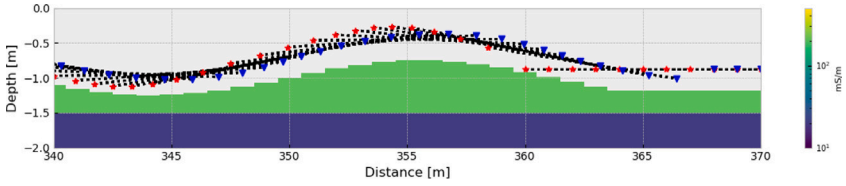

Fig. 22. Rigid boom position for positions at distance X = 340–370 m. Red star: transmitter position. Blue triangle: receiver position at 8 m offset. Dotted line: rigid boom. The midpoint of the boom is located 0.3 m above the air-surface interface. The instrument pitch angle is tangent to the slope. Due to the increasingly undulating topography and rigidity of the boom, there will be a larger vertical air-surface interface distance from the transmitter or receiver coil in some positions.

different cross-sections, presented in the Supplementary Material (Carrizo Mascarell et al., 2025). The higher inaccuracies are located in the transitions from channel bars to river plains, due to the effect in the measurements to lateral changes in the model parameters, which are also clear in the misfit between the 1D and 3D responses in Fig. 27 in these positions. The fit between the LCI and PWI estimated and true response is below 10% error.

Example 5. Channel feature with topography

This example presents the previous 3D channel feature in a soft valley topography, which is presented in Fig. 28. The computed measurements were obtained using 3D forward modelling assuming the instrument positioning parallel to the air-subsurface interface (as in Case (c)). The results of the PWI and LCI estimated models are presented in Figs. 29 and 30. In the maps and cross-section of the estimated models, it is clear that both PWI and LCI methods provide similar results for the model parameters. Both inversion methodologies are significantly affected by the topography effects in the measurements. The breakdown of the estimations with increasing topography is observed in the worsening of the estimated models from crossline Y = 10 m to crossline Y = 30 m, due to the topography valley becoming narrower in that direction, and thus, larger dips. Moreover, comparing the responses misfits in Figs. 31 and 32 it is clear that in the Y = 30 m crossline, the difference between 1D forward-modelled and 3D

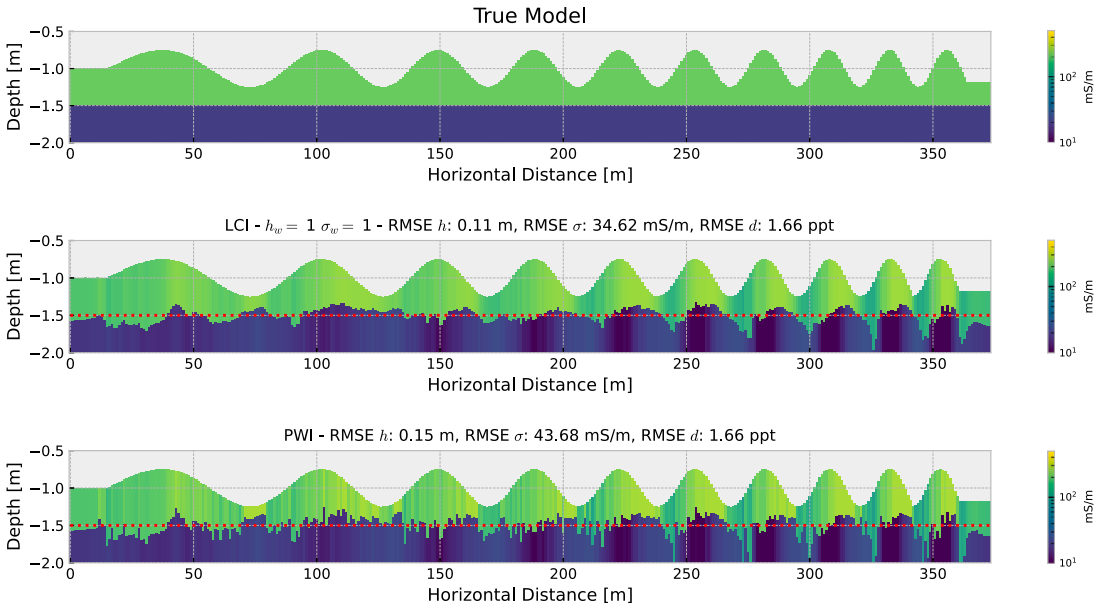

Fig. 23. Results of inversion methods for an increasing dip of the air-subsurface interface. Top: True model. Middle: LCI estimated model. Bottom: PWI estimated model. RMSE values of the estimated model parameters are presented.

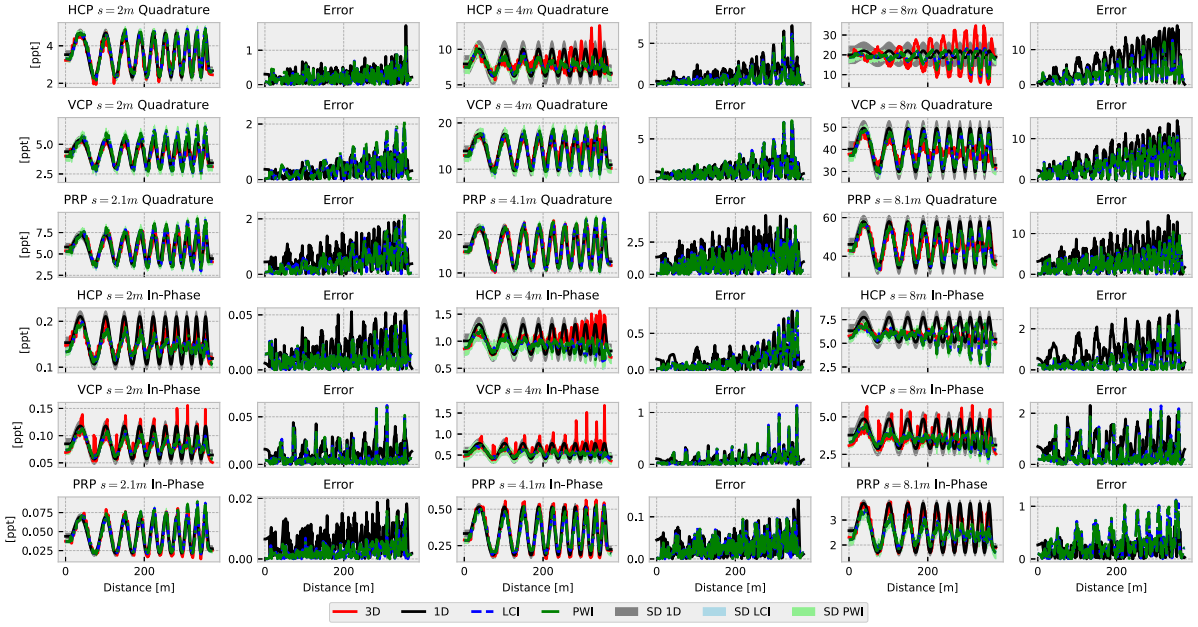

Fig. 24. Measurements corresponding to the model in Fig. 23 for all coil configurations and measurement components. The difference percentage with 3D measurements is shown below each measurement.

forward-modelled responses increases largely. Neither the PWI or the LCI methods correspond accurately to the true responses.

Case study: Ackerdijkse plassen

We applied both inversion methods for FDEM data acquired in the natural monument Ackerdijkse Plassen, The Netherlands (see Fig. 33). This area shows a sandy channel deposit feature embedded in peat-silt plains in satellite images and nearby borehole data. In this case, we used only the HCP and VCP coil geometries in the methodology. For offsets up to 4 m, the *in-phase* values are considered less accurate according to the FDEM instrument manufacturer so these were not included in the estimations (Taylor, 2023). The data was acquired holding the rigid-boom parallel to the topography dip, with the midpoint at a fixed height from the air-subsurface. The topography of the area is shown in Fig. 34.

The acquired data was inverted using the PWI and LCI methodologies. Cross-sections and maps of the estimated models are shown in Figs. 35 and 36. From the cross-section results, we deduce that both inversion methods obtain similar electrical conductivity values of the layers and thickening of a channel feature in the centre area of the cross-sections. However, the LCI method presents a smoother estimated model, with transitional changes with respect to the thicknesses and electrical conductivities. We consider that this is an advantage of the LCI method since it provides more stable solutions with respect to the noise present in the data, which creates a laterally inconsistent estimated model in PWI results. In Figs. 37 and 38, the field measurements and the estimated responses are compared. As expected, the 1D

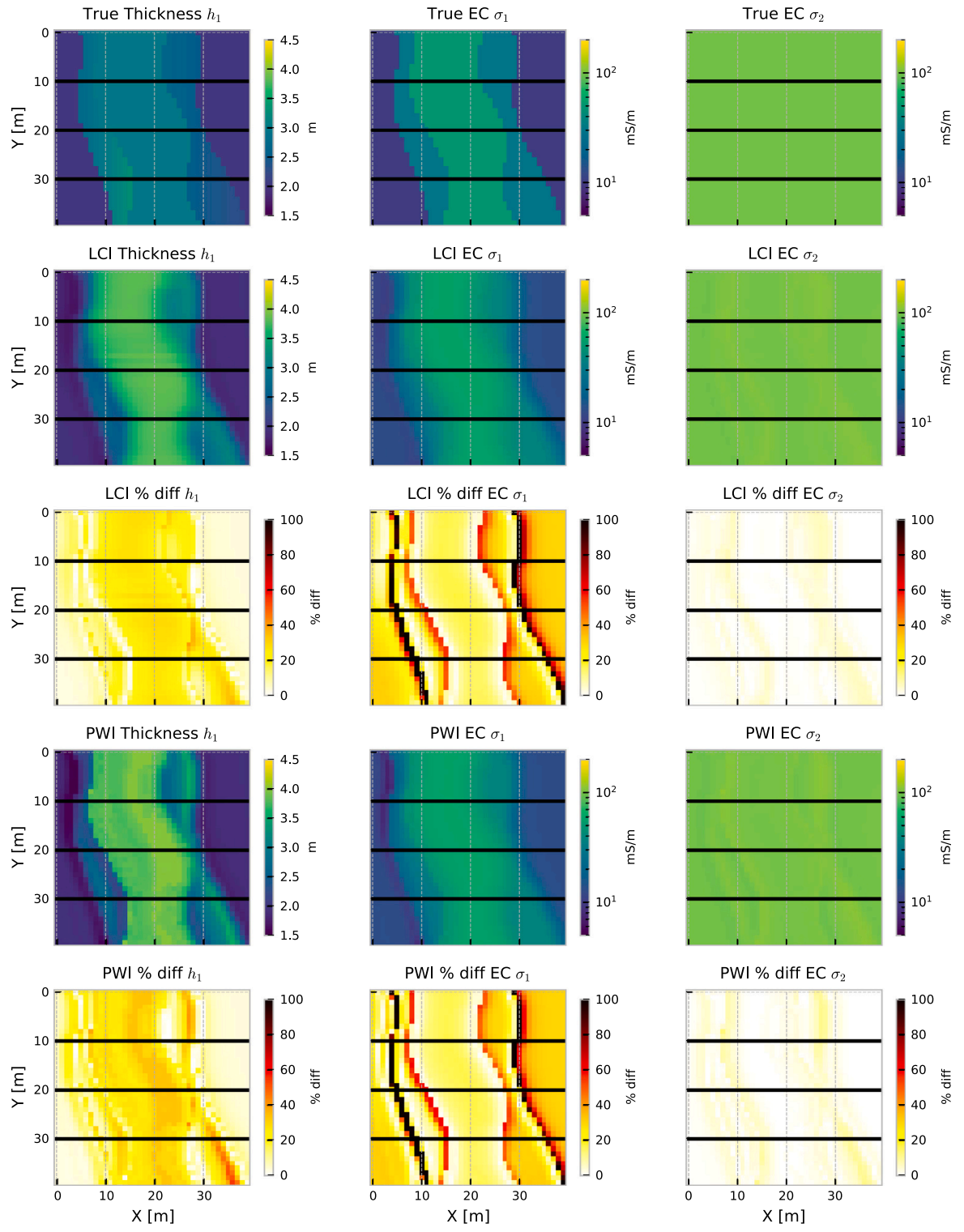

Fig. 25. Maps of model parameters in Channel example. Top row: True model parameters. Second and fourth row: Maps of the LCI and PWI estimated model parameters. Third and fifth row: Maps of the difference percentage between true and estimated models. The position of cross sections is indicated with black lines.

forward-modelled responses differ from the true measurements, which were acquired by infringing the assumptions.

The resulting responses reproduce the HCP and VCP, both 2 m and 4 m coil separation *quadrature* measurements. However, they do not reproduce the field measurements in the HCP *quadrature* at 8 m offset coil geometry. It is difficult to determine the reason, which could be due to 3D variations of the electrical conductivity or additional layers not considered in the parameterization of the inverse problem. The *in-phase* responses are reproduced with errors from 10%–20%. We know that some distortions caused by the dipping topography and the instrument pitch are being propagated into the estimation of the model. However, since the distribution of electrical conductivity in the area is not known with certainty it is difficult to quantify the exact influence of breaking the 1D forward modelling assumptions in this case.

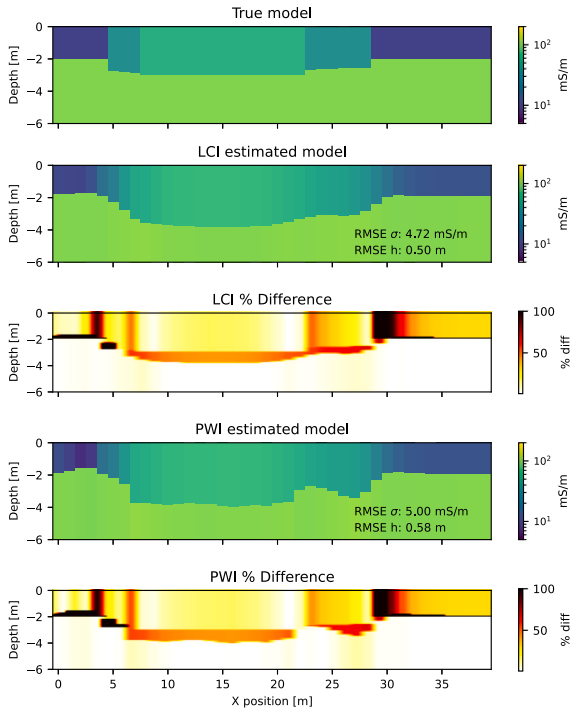

Fig. 26. Inversion results at crossline Y = 10 m from channel feature example. Top row: True model. Second and fourth row: LCI and PWI estimated models. Third and fifth row: difference percentage between true and estimated model.

6. Discussion of results

In Section 4, we presented several examples where the assumptions of the 1D forward function are violated. Cases (b) and (c) show that the pitch angle of the instrument and topographical variations can notably affect the measurements in both *quadrature* and *in-phase* components, particularly in the VCP *quadrature* and PRP *in-phase* parts. Furthermore, case (d) showed that the dip of the second interface also impacts the measurements, especially the VCP and PRP *in-phase* parts. In cases (c) and (d), it is clear from Figs. 5–7, that the *in-phase* component is the most affected by the breakdown of the 1D forward function.

To determine how far these measurement distortions affect the model estimations, we applied the PWI and LCI methods to several numerical examples shown in Section 5. Although the results of case (d) show large distortions in the *in-phase* measurements for all the model contrasts, the estimation results of both PWI and LCI methods in example 1 are sufficient to solve 2-layered earth models accurately. This is true when measurements are acquired without topography, the assumption of instrument positioning parallel to the air-surface interface holds, and the second interface dip is not greater than 7.5°. This is also clear in example 2, where with increasing dip of the second interface, the inversion results worsen. The LCI methodology presents little to no advantage with respect to estimation accuracy. In Fig. 19, the results show that both PWI and LCI are affected by the effects of 2D lateral variability. While the PWI can overall estimate the position of the first layer thickness, the results also present spurious estimations. On the other hand, while LCI does not resolve properly the first layer thickness, it provides smooth and more stable electrical conductivity estimations.

From the results in Fig. 4, we observe that in a data acquisition scheme where the instrument is held horizontally, a dipping air-subsurface interface at an angle greater than 2° can distort the measurements in all coil configurations and components. This is also demonstrated by both the results of PWI and LCI in example 3 (Fig. 23), where the inversion results worsen with increasing undulation of the air-subsurface interface. The PWI results show poor first-layer thickness estimations, even with slight topography variations, and worsening in the electrical conductivities as the dip increases. Moreover, LCI provides a better first-layer thickness estimation but, like PWI, exhibits declining accuracy in electrical conductivity values with increasing dip.

Examples 4 and 5, which include a 3D channel feature, also illustrate very clearly the effect of a dip in the topography. In example 4, where there is no topography influence, the PWI and LCI estimations and responses did not diverge significantly from the true values. The largest errors were only present where there were lateral conductivity variations. However, in example 5, imposing on the model a very soft topography made the measurements diverge significantly, causing poor results of the model estimations. Comparing all the geometry cases and their error propagation in the numerical examples, we consider that case (c) shows the largest impact. The breakdown of both assumptions creates distortions larger than 10% with only 2° dip in all the coil configuration *in-phase* measurements and in the VCP *quadrature* measurement, which increased with the resistivity of the halfspace.

The resulting estimations of the case study are quite similar for both PWI and LCI methods in terms of electrical conductivity values. In both, the channel feature can be observed in the first layer. The thickness of the first layer varies smoothly in the LCI results. We presume that the spiky nature of the thickness of the first layer for the PWI estimated model can result from noise in the data. We consider that LCI can be used to obtain smoother estimations of the model parameters when noise is present in the data, which is very common in field cases. Nonetheless, we must be careful with the geological setting where this algorithm is applied since LCI assumes that lateral variations of the parameters are smooth.

In this case study, it is not possible to determine whether the discrepancies between the PWI and LCI responses and the true measurements arise from topographic variations or from other factors, such as noise. It is also likely that the imposed 2-layer model parameterization does not accurately represent the complexity of a three-dimensional earth. Consequently, we cannot quantify the influence of topography and pitch angle on the measurements, nor assess the extent to which these factors affected the model estimations. Even so, the numerical examples showed that there must be errors in the estimations due to the presence of topography and holding the instrument parallel to the dipping ground surface. Both PWI and LCI estimations are likely not reproducing the true distribution, partly due to the measurement distortions.

This analysis demonstrates that while both PWI and LCI can provide reasonable estimations, under ideal acquisition conditions, their accuracy decreases significantly when measurements are affected by topography, pitch angle, or subsurface complexity. Relying on 1D forward functions in the presence of 3D effects not only amplifies errors in the estimations but also increases the potential non-uniqueness of the inversion problem. These observations highlight the importance of accounting for acquisition geometry and geological complexity when interpreting inversion results. Future work should focus on integrating topographic and orientation corrections directly into the inversion process or developing approaches that introduce the acquisition and geological geometry.

7. Conclusions

The analysis demonstrates that deviations from the 1D forward modelling assumptions, particularly instrument tilt, topographic undulations, and layer dips, can significantly distort frequency domain electromagnetic induction measurements, with the severity increasing as these factors become more pronounced. These deviations are propagated into the inversion results. Both piecewise and laterally constrained inversion methods can produce accurate results for flat topography, gentle slope 2-layered earth models, but their performance deteriorates in the presence of topography (larger than 2°) or drastic

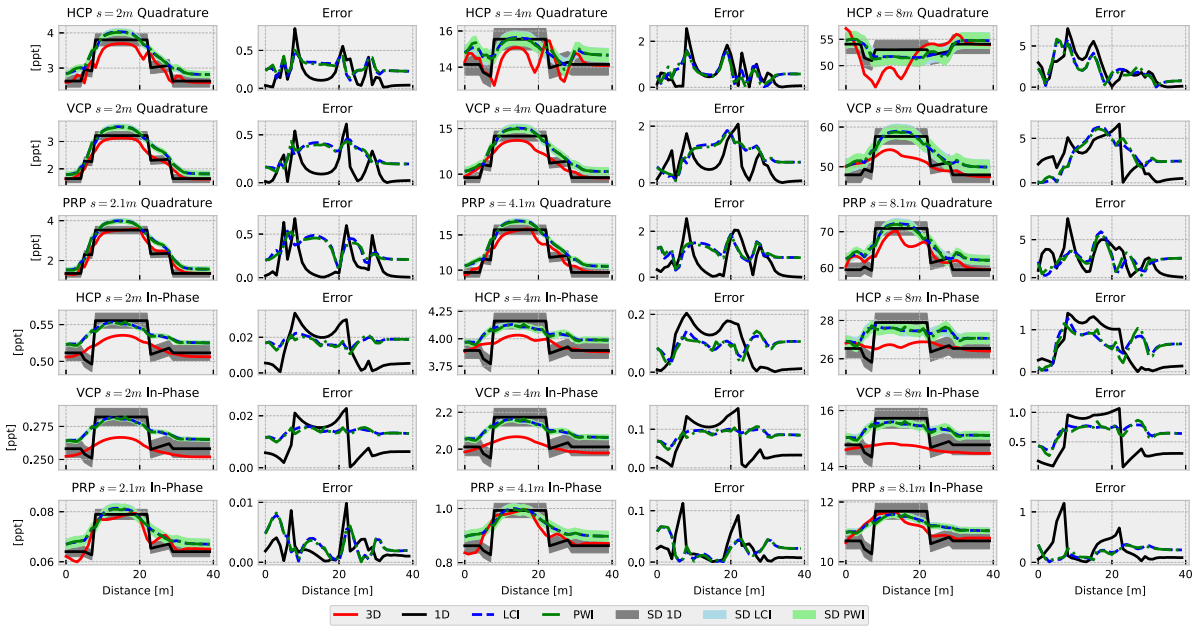

Fig. 27. Measurements corresponding to the estimated models presented in Fig. 26. 3D Channel feature example.

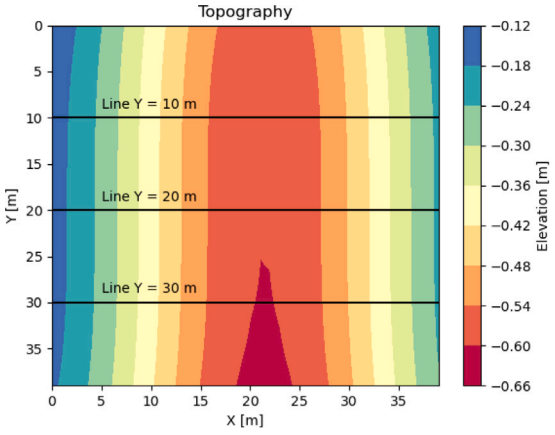

Fig. 28. Topography map of a valley for the numerical example of a 3D Channel.

lateral conductivity variations. Piecewise inversion tends to estimate first-layer thickness more precisely but suffers from spurious or spiky outputs in the presence of measurement distortions or noise. On the other hand, laterally constrained inversion produces smoother and more stable conductivity estimates, especially in noisy data, although with reduced thickness accuracy. Neither method fully compensates for strong 2D/3D effects, and the reliability of both depends heavily on the geological setting and acquisition conditions. Therefore, care must be taken to assess the assumptions considered before applying these inversion approaches to real-world surveys. It is possible that for strongly 3D varying geological settings, topography/pitch-angle corrections or a 2D/3D inversion methodology should be used. The findings show the importance of developing realistic yet computationally efficient forward modelling and inversion methods that can account for complex acquisition conditions in frequency-domain electromagnetic induction surveys.

CRediT authorship contribution statement

Maria Carrizo Mascarell: Writing – original draft, Visualization, Methodology, Investigation, Conceptualization. **Dieter Werthmüller:** Writing – review & editing, Supervision, Software. **Evert Slob:** Writing – review & editing, Supervision, Methodology, Funding acquisition, Conceptualization.

Declaration of competing interest

The authors declare the following financial interests/personal relationships which may be considered as potential competing interests: Evert Slob reports financial support was provided by WarmingUP. If there are other authors, they declare that they have no known competing financial interests or personal relationships that could have appeared to influence the work reported in this paper.

Acknowledgments

This project was carried out as part of the WarmingUP Innovation Plan, made possible partially by a subsidy from the Rijksdienst voor Ondernemend Nederland (RVO) in the context of the Meerjarige Missiegedreven Innovatie Programma's (MMIP) subsidy scheme (RVO project number TEUE819001).

Data availability

Data will be made available on request.

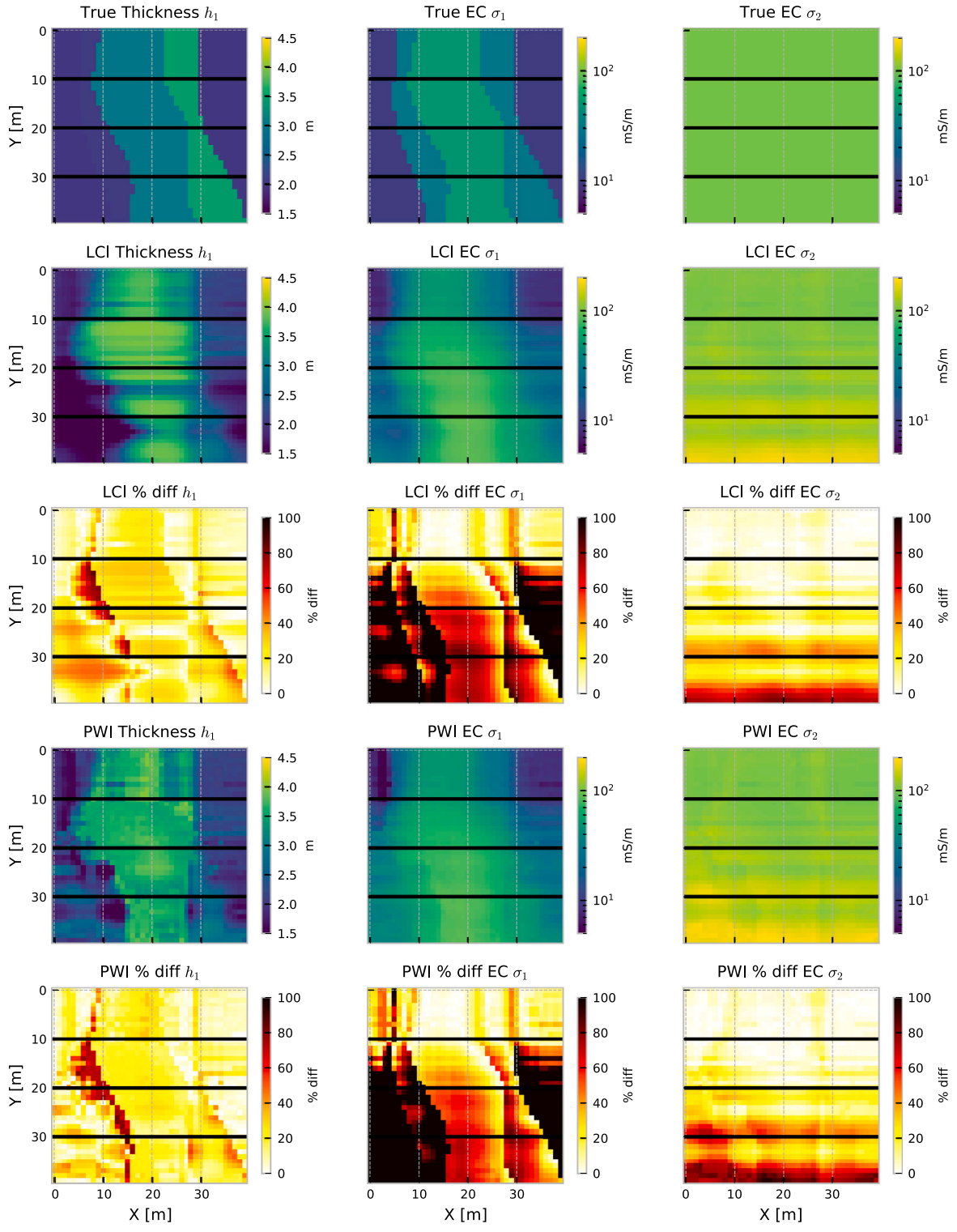

Fig. 29. Maps of model parameters for the 3D channel example with topography. The position of the cross-sections is indicated with a black line.

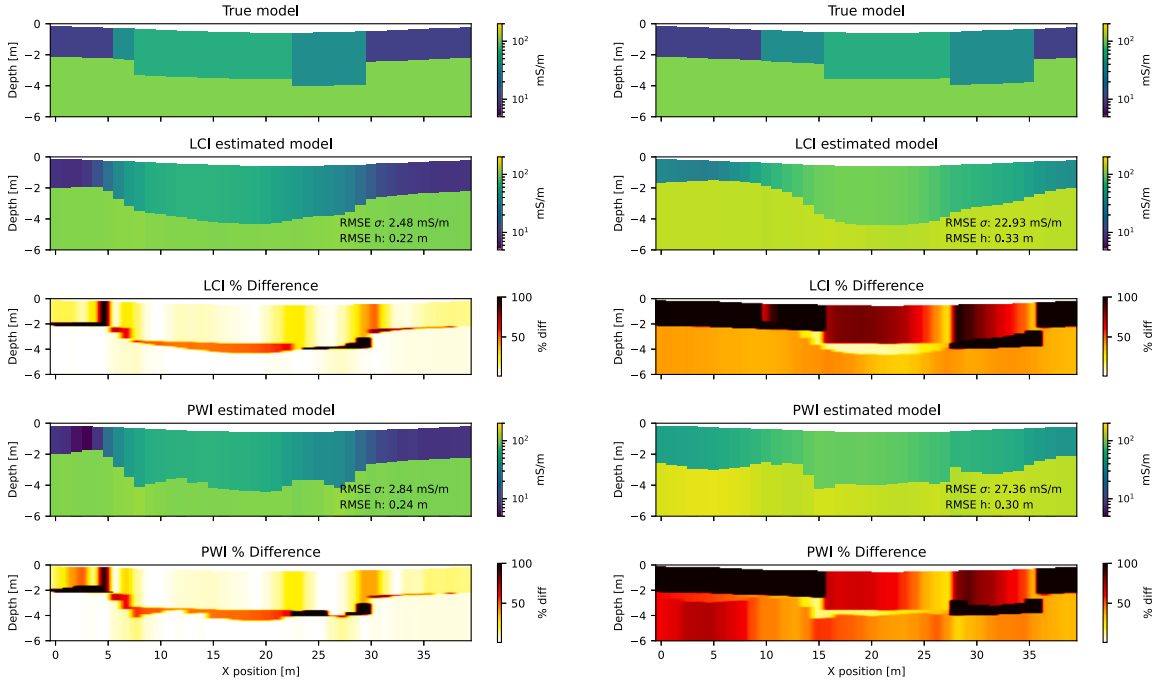

(a) Cross-section at Y = 10 m. (b) Cross-section at Y = 30 m.

Fig. 30. Inversion results at two cross-sections for a 3D channel feature in a valley topography. The cross-section at Y = 10 m presents better results than the cross-section at Y = 30 m, where the valley is narrower and the dips are larger.

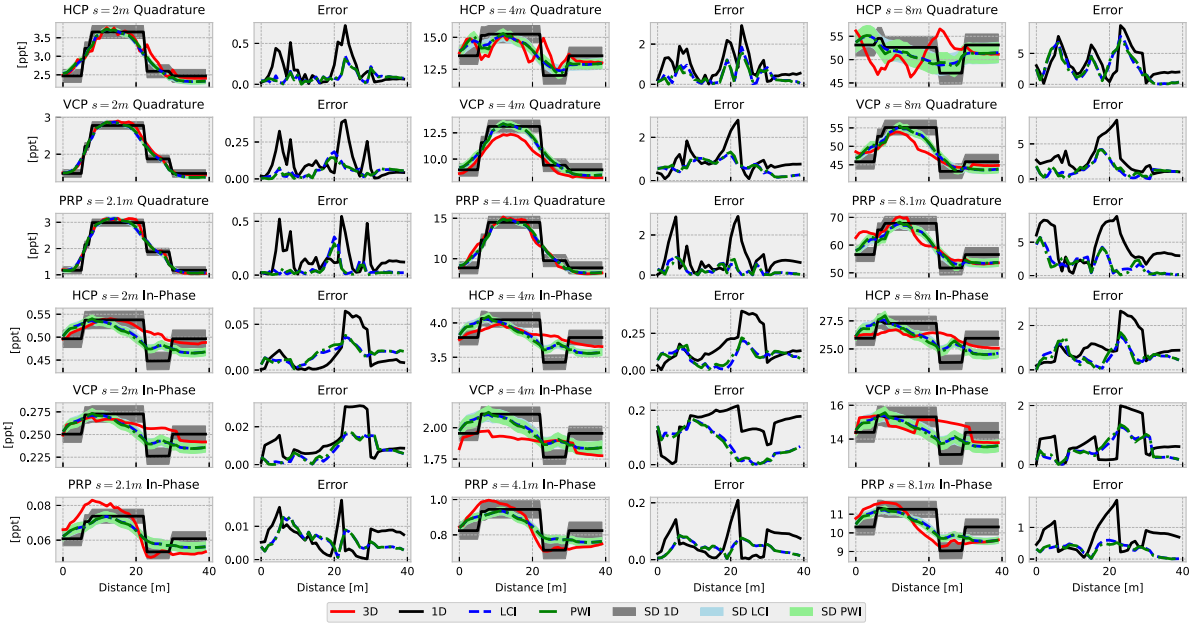

Fig. 31. Measurements corresponding to the estimated models of cross-section Y = 10 m presented in Fig. 30. 3D Channel feature with topography example.

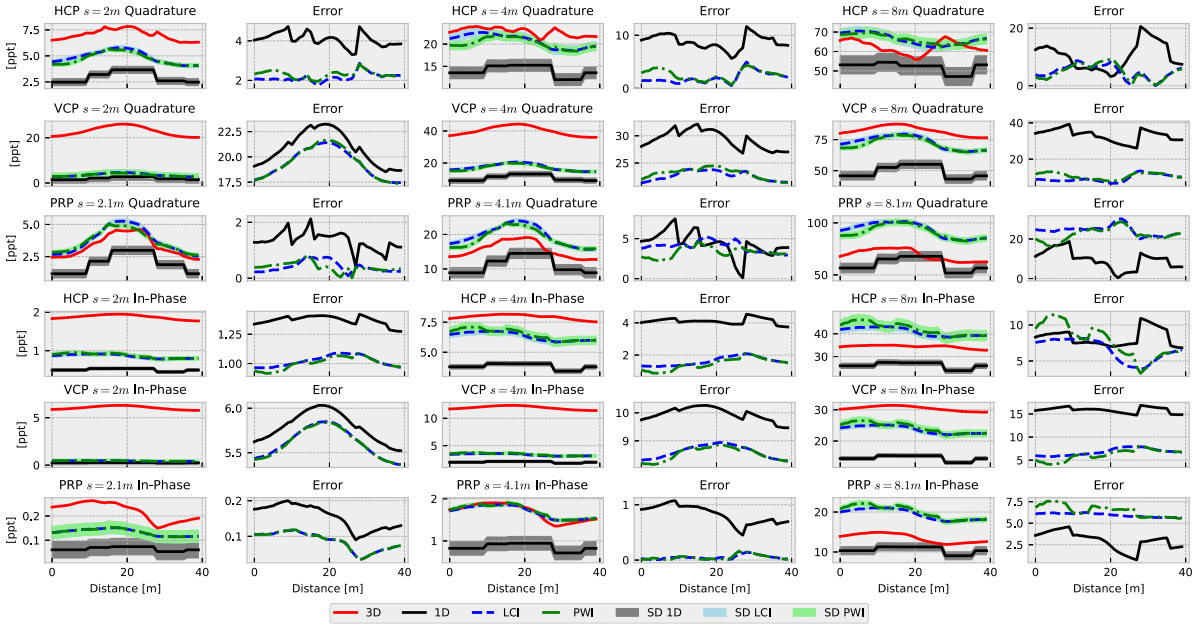

Fig. 32. Measurements corresponding to the estimated models of cross-section Y = 10 m presented in Fig. 30. 3D Channel feature with topography example.

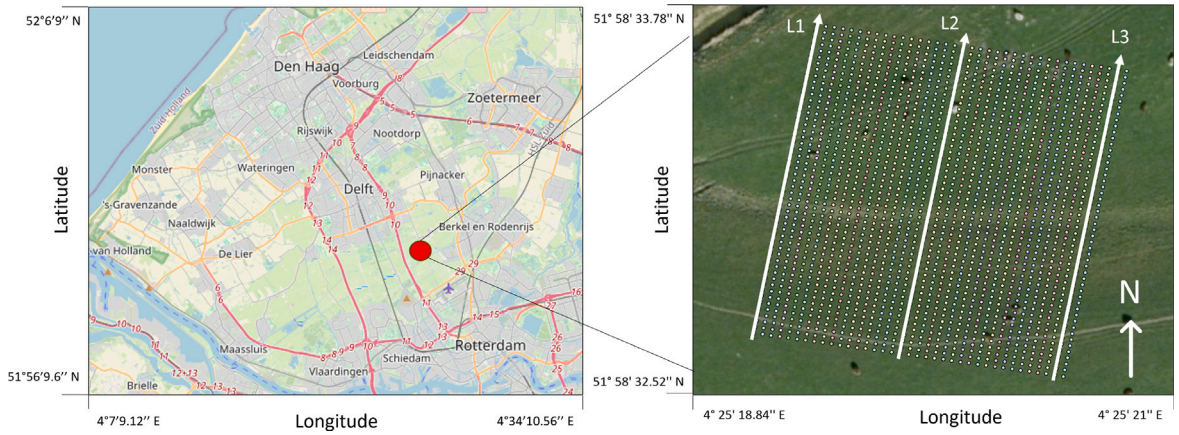

Fig. 33. Left: Map of the Rotterdam — The Hague area, Ackerdijkse Plassen natural monument marked with red dot. Right: FDEM measurements and position of cross-sections. (For interpretation of the references to colour in this figure legend, the reader is referred to the web version of this article.)

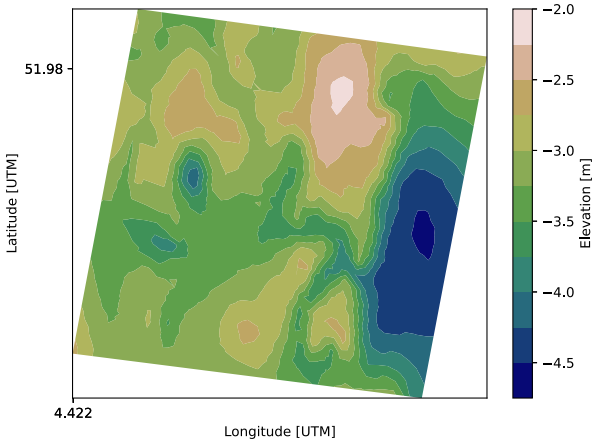

Fig. 34. Topography map of the Field study area.

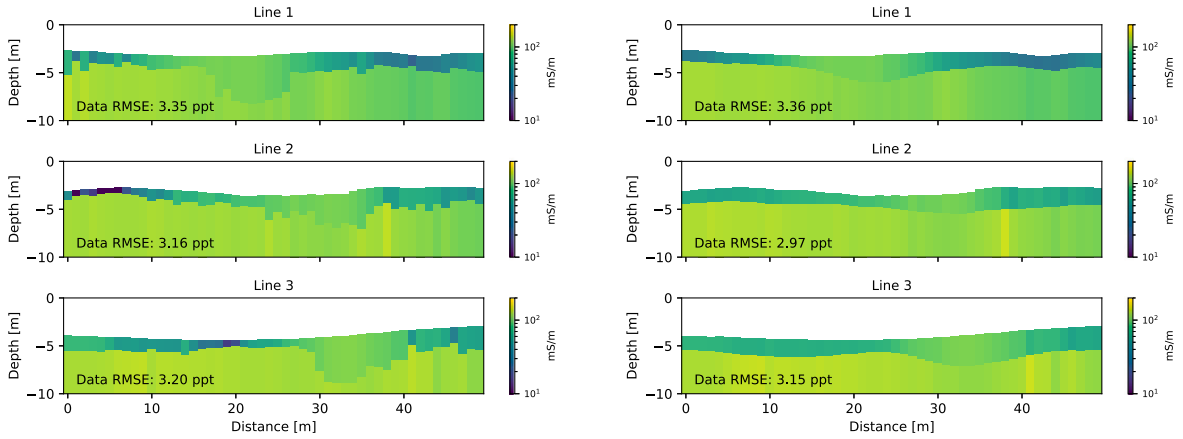

Fig. 35. Left: Cross-sections of the models estimated with PWI. Right: Cross-sections of the models estimated with LCI. RMSE values of the estimated responses are presented. The positions of these cross-sections are shown in Fig. 33.

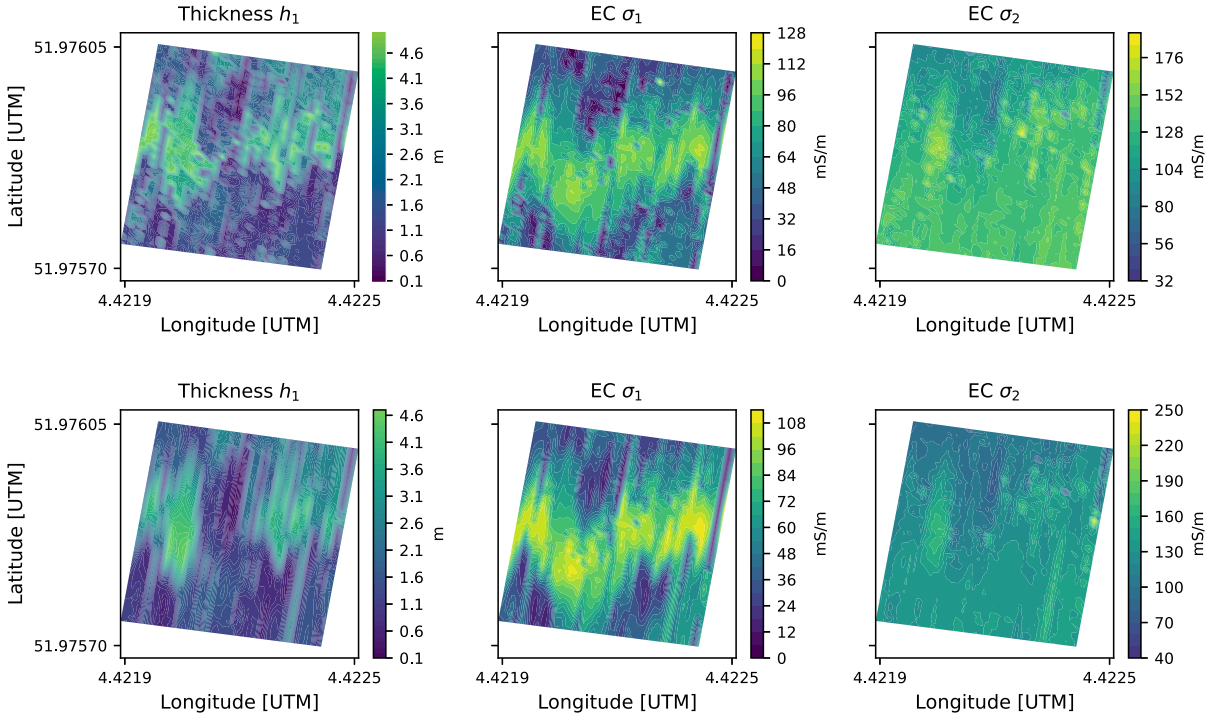

Fig. 36. Top: Maps of model parameters estimated with PWI. Bottom: Maps of model parameters estimated with LCI. The results show similar estimations overall with both inversion methods.

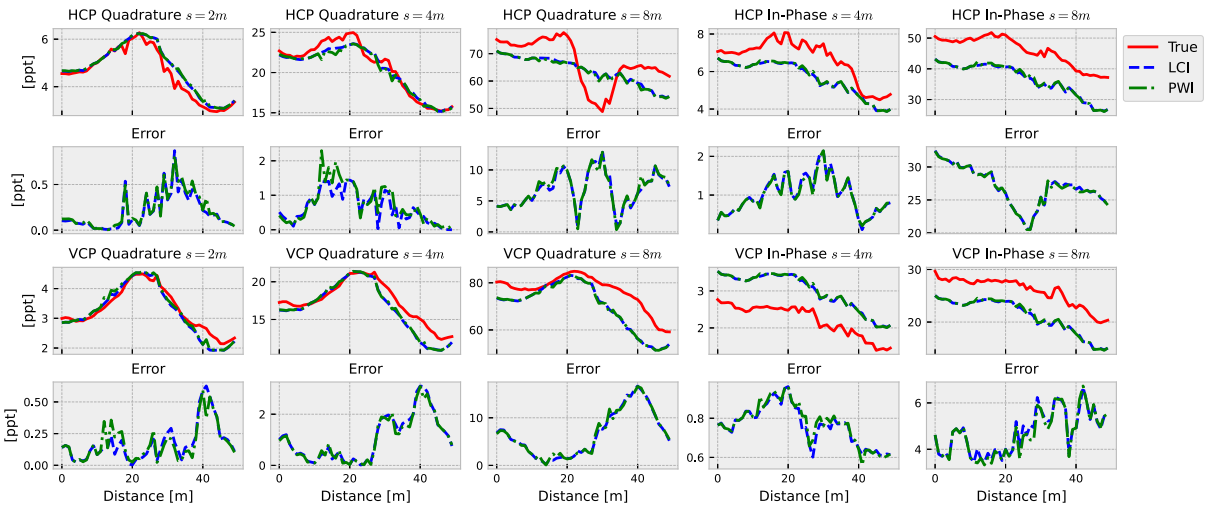

Fig. 37. Data fit of the inversion results of Line 1 in Fig. 35. Red line: Field measurements. Blue dashed line: LCI response. Green dashed line: PWI response.

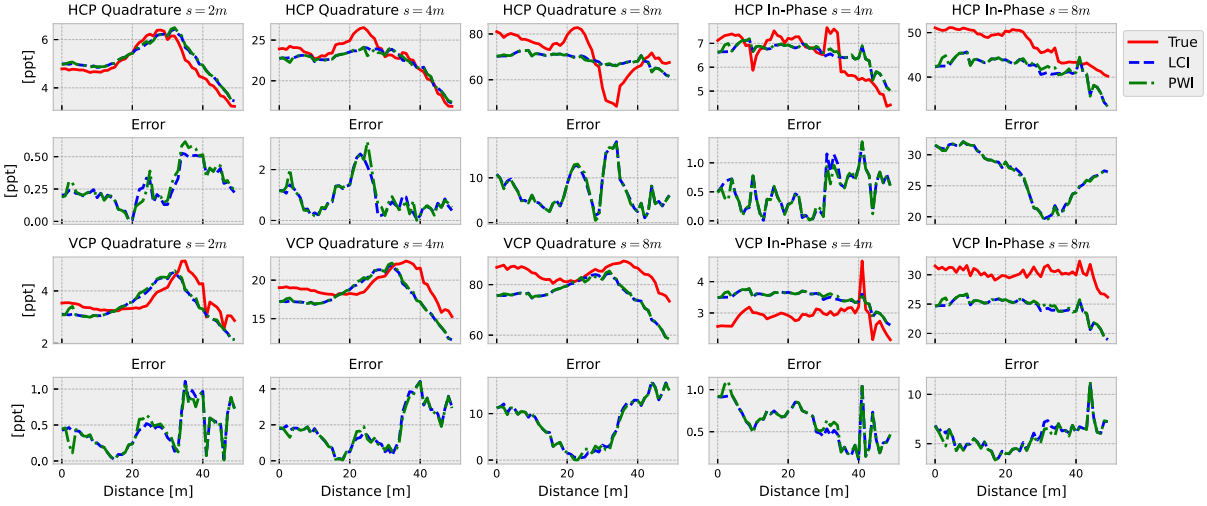

Fig. 38. Data fit of the inversion results of Line 3 in Fig. 35. Red line: Field measurements. Blue dashed line: LCI response. Green dashed line: PWI response.

References

Alumbaugh, D.L., Newman, G.A., 2000. Image appraisal for 2-D and 3-D electromagnetic inversion. Geophysics 65 (5), 1455–1467. http://dx.doi.org/10.1190/1.1444834.

Auken, E., Christiansen, A.V., 2004. Layered and laterally constrained 2D inversion of resistivity data. Geophysics 69 (3), 752–761. http://dx.doi.org/10.1190/1.1759461.

Auken, E., Christiansen, A.V., Jacobsen, B.H., Foged, N., Sorensen, K.I., 2005. Piecewise 1D laterally constrained inversion of resistivity data. Geophys. Prospect. 53 (4), 497–506. http://dx.doi.org/10.1111/j.1365-2478.2005.00486.x.

Bai, P., Vignoli, G., Hansen, T.M., 2021. 1D Stochastic inversion of airborne time-domain electromagnetic data with realistic prior and accounting for the forward modeling error. Remote. Sens. 13 (19), http://dx.doi.org/10.3390/rs13193881.

Carrizo Mascarell, M., Riakhi, F., Slob, E., Werthmüller, D., Van Breukelen, B., 2024a. Integrating electromagnetic induction measurements and electrical resistivity tomography to monitor rainwater lenses in dutch polders. In: NSG 2024 30th European Meeting of Environmental and Engineering Geophysics. Vol. 2024, pp. 1–5. http://dx.doi.org/10.3997/2214-4609.202420119.

Carrizo Mascarell, M., Werthmüller, D., Slob, E., 2024b. Estimation of electrical conductivity models using multi-coil rigid-boom electromagnetic induction measurements. Comput. Geosci. 193, http://dx.doi.org/10.1016/j.cageo.2024.105732.

Carrizo Mascarell, M., Werthmüller, D., Slob, E., 2025. Supplementary material: Additional results. http://dx.doi.org/10.5281/zenodo.17670207.

Christiansen, A., Pedersen, J., Auken, E., Søe, N., Holst, M., Kristiansen, S., 2016. Improved geoarchaeological mapping with electromagnetic induction instruments from dedicated processing and inversion. Remote. Sens. 8 (12), 1022. http://dx.doi.org/10.3390/rs8121022.

Constable, S., Parker, R., Constable, C., 1987. Occam's inversion: a practical algorithm for generating smooth models from electromagnetic sounding data.. Geophysics 52 (3), 289–300. http://dx.doi.org/10.1190/1.1442303.

Deleersnyder, W., Dudal, D., Hermans, T., 2022. Novel airborne EM image appraisal tool for imperfect forward modeling. Remote. Sens. 14 (22), http://dx.doi.org/10.3390/rs14225757.

Günther, T., Rücker, C., Spitzer, K., 2006. Three-dimensional modelling and inversion of DC resistivity data incorporating topography — II. inversion. Geophys. J. Int. 166 (2), 506–517. http://dx.doi.org/10.1111/j.1365-246X.2006.03011.x.

Heagy, L.J., Cockett, R., Kang, S., Rosenkjaer, G.K., Oldenburg, D.W., 2017. A framework for simulation and inversion in electromagnetics. Comput. Geosci. 107, 1–19. http://dx.doi.org/10.1016/j.cageo.2017.06.018.

Kiyan, D., Rath, V., Muller, M.R., Ture, M.D., Hodgson, J., 2022. 1-D inversion of frequency-domain airborne electromagnetic data using the open-source aempy toolbox. J. Appl. Geophys. 198, 104562. http://dx.doi.org/10.1016/j.jappgeo.2022.104562.

Klose, T., Guillemoteau, J., Vignoli, G., Tronicke, J., 2022. Laterally constrained inversion (LCI) of multi-configuration EMI data with tunable sharpness. J. Appl. Geophys. 196, 104519. http://dx.doi.org/10.1016/j.jappgeo.2021.104519.

Ley-Cooper, A.Y., Macnae, J., Viezzoli, A., 2010. Breaks in lithology: Interpretation problems when handling 2D structures with a 1D approximation. Geophysics 75 (4), WA179–WA188. http://dx.doi.org/10.1190/1.3483101.

McLachlan, P., Blanchy, G., Binley, A., 2021. Emagpy: Open-source standalone software for processing, forward modeling and inversion of electromagnetic induction data. Comput. Geosci. 146, 104561. http://dx.doi.org/10.1016/j.cageo.2020.104561.

McNeill, J., 1980. Electromagnetic Terrain Conductivity Measurement at Low Induction Numbers. Tech. Note TN-6 15.

Monteiro Santos, F.A., 2004. 1-D laterally constrained inversion of EM34 profiling data. J. Appl. Geophys. 56 (2), 123–134. http://dx.doi.org/10.1016/j.jappgeo.2004.04.005.

Nocedal, J., Wright, S.J., 1999. Nonlinear least-squares problems. In: Numerical Optimization. Springer New York, New York, NY, pp. 250–275. http://dx.doi.org/10.1007/0-387-22742-3_10.

Oldenburg, D.W., Heagy, L.J., Kang, S., Cockett, R., 2020. 3D electromagnetic modelling and inversion: a case for open source. Explor. Geophys. 51 (1), 25–37. http://dx.doi.org/10.1080/08123985.2019.1580118.

Rücker, C., Günther, T., Wagner, F.M., 2017. Pygimli: An open-source library for modelling and inversion in geophysics. Comput. Geosci. 109, 106–123. http://dx.doi.org/10.1016/j.cageo.2017.07.011.

Silic, J., Paterson, R., FitzGerald, D., Archer, T., 2015. Comparing 1D and 2.5D AEM inversions in 3D geological mapping using a new adaptive inversion solver. In: 14th International Congress of the Brazilian Geophysical Society & EXPOGEF, Rio de Janeiro, Brazil, 3-6 August 2015. pp. 184–189. http://dx.doi.org/10.1190/sbgf2015-036.

Taylor, R., 2023. EM induction. URL: https://dualem.com/documents/em-induction/.

Thalhammer, M., 2022. Imaging of active layer characteristics through quasi-3D inversion of frequency-domain electromagnetic soundings. URL: http://resolver.tudelft.nl/uuid:1a311a47-6f15-42c0-86e0-4b7a75ddc2cd.

Wait, J.R., 1982. Chapter III - Electromagnetic Induction and Loop–Loop Coupling. In: Wait, J.R. (Ed.), Geo-Electromagnetism. Academic Press, pp. 101–139. http://dx.doi.org/10.1016/B978-0-12-730880-7.50007-7.

Werthmüller, D., 2017. An open-source full 3D electromagnetic modeler for 1D VTI media in Python: empymod. Geophysics 82 (6), WB9–WB19. http://dx.doi.org/10.1190/geo2016-0626.1.

Werthmüller, D., Mulder, W.A., Slob, E.C., 2019. Emg3d: A multigrid solver for 3D electromagnetic diffusion. J. Open Sour. Softw. 4 (39), 1463. http://dx.doi.org/10.21105/joss.01463.

Zhang, B., Engebretsen, K., Fiandaca, G., Cai, H., Auken, E., 2021. 3D inversion of time-domain electromagnetic data using finite elements and a triple mesh formulation. Geophysics 86 (3), E257–E267. http://dx.doi.org/10.1190/geo2020-0079.1.